

## Simulation of Mesoscale Variability in the Gulf of Mexico: Sensitivity Studies, Comparison with Observations, and Trapped Wave Propagation

LIE-YAUW OEY

*Program in Atmospheric and Oceanic Sciences, Princeton University, Princeton, New Jersey*

(Manuscript received 28 March 1994, in final form 27 April 1995)

### ABSTRACT

A primitive equation Gulf of Mexico model was used to examine variability of the Loop Current (LC) and Loop Current eddies (LCE). Realistic results were obtained for a certain range of values of the horizontal mixing coefficient: eddy paths were west and southwestward; eddy propagation speeds from 3 to 5 km day<sup>-1</sup>; the ratio of minor to major eddy axes about 0.8; eddy shedding periods from 200 to 500 days; eddy lifetimes from 100 to 200 days; eddy sizes from 200 to 400 km; and eddy swirl transports, as fractions of the specified inflow of 30 Sv, were from 0.55 to 0.85. On the other hand, the maximum vertical deepening of the 20°C isotherm was 15% to 50% less than that observed, resulting in weaker near-surface currents of about 0.65 m s<sup>-1</sup>, in comparison to observed values of 0.88 to 1.7 m s<sup>-1</sup>. A strong correlation between eddy shedding and decreasing or reversing lower-layer (below 750 m) transport in the Yucatan Channel is found. In the western Gulf, current variability is produced by eddy arrivals, as well as by forcing due to bottom-intensified topographic Rossby waves, which propagate along the slope from the east with a group velocity of about 12 km day<sup>-1</sup> and periods of about 30–100 days. These waves are generally preceded by faster coastally trapped wave propagation, and all are produced by LC pulsation, eddy shedding, and westward propagation.

### 1. Introduction

Hurlburt and Thompson (1980) studied the Loop Current (LC) and Loop Current eddies (LCE) in the Gulf of Mexico using two-layer and reduced-gravity models, covering a wide range of model parameters and forcing, and showed that periodic eddy shedding was obtained with steady inflow. A similar level of parametric and forcing study with a three-dimensional model is beyond the scope of this paper. Nevertheless, an investigation into the sensitivity of the model solutions to horizontal viscosity and diffusivity coefficients and boundary forcing, limited though it may be, is warranted. The sensitivity experiments will provide guidance as to what a “best tuned” solution is for a shelf circulation study with Gulf-scale forcing, for example, or for data assimilation of the LC and LCEs. Moreover, the model used here does not specify boundary conditions at the Yucatan Channel and Straits of Florida, and may therefore give rise to different physics from other models that do. Indeed, Hurlburt and Thompson (1980) found no eddy shedding when either a landmass was used in place of the Florida shelf, arguably justified in a reduced-gravity model (see their Fig. 17), or when

bottom inflow through the Yucatan Channel was increased (see their Fig. 26) in a two-layer model with realistic topography. In the latter case, eddy shedding resumed if the west Florida slope was (unrealistically) moved eastward or if the Yucatan bottom inflow was reduced. Hurlburt and Thompson also found unrealistically weak eddies with a two-layer flat-bottom model, because of rapid loss of energy through baroclinic instability to the deep layer, while more realistic eddies were found when topography was included. Thus, it is not clear if a model with more realistic topography can produce eddy shedding since this depends on rather intricate dynamics, which the model must simulate.

Our ultimate objective is to produce a high-resolution simulation of the circulation and mixing over the Louisiana–Texas (LATEX) shelf with detailed topography and forcing. Much debate has centered on the importance of Gulf-scale forcing on shelf processes (e.g., Oey 1995), since this dictates the design of either a limited-area shelf domain, or a larger Gulf domain with high resolution over the shelf. To assess the Gulf’s effects, we decided to design a model that encompasses the entire Gulf. This paper describes the model, boundary conditions, and modeling strategy, and concentrates on the Gulf-scale responses and how they compare with observations. Follow-up papers will examine how and to what extent the shelf processes are affected by eddies over the slope and in the Gulf.

The paper is organized as follows. Section 2 describes the model and forcing. Section 3 presents the

---

Corresponding author address: Dr. Lie-Yauw Oey, Program in Atmospheric and Oceanic Sciences, Princeton University, Sayre Hall, Forrester Campus, Princeton, NJ 08544.  
E-mail: lyo@kuroshio.princeton.edu

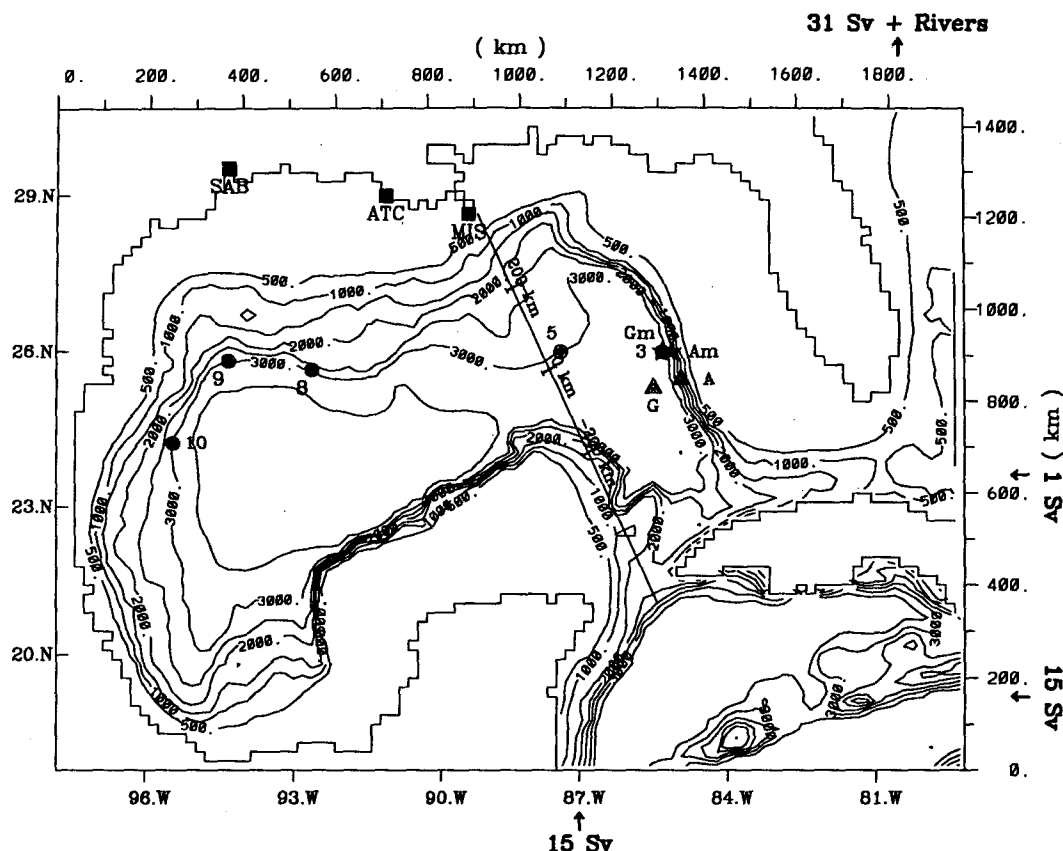


FIG. 1. The Gulf of Mexico model domain and isobaths in meters; squares indicate river discharge points. MIS: Mississippi, ATC: Atchafalaya, SAB: Sabine plus others. Circles denote stations where model currents are analyzed in text. Triangles are Hamilton's (1990) current moorings, and stars the nearest model moorings (Table 2). Model station 3 is on the 3000-m isobath, while Gm is slightly offshore on the 3200-m isobath.

results and sensitivity experiments. Section 4 compares the model results with published observations and gives evidence of bottom-trapped topographic Rossby wave (TRW) and coastally trapped wave (CTW) propagation in the model. Section 5 is a concluding summary.

## 2. The model

### a. The model domain

The model domain (Fig. 1) includes the Gulf, the northwestern portion of the Caribbean basin, and the southwestern portion of the South Atlantic Bight. The inflow location in the Caribbean is preferred instead of that at the Yucatan Channel. The latter would constrain the model solution. The outflow is specified at approximately 30°N off the South Atlantic Bight rather than at the Straits of Florida off the Keys (81°W). Observations show the existence of cyclones in the vicinity of Dry Tortugas [24°N, 82°–83°W; Vukovich et al. (1979)], which may be relevant to LCE shedding dynamics. Our domain allows for the free development of such cyclonic perturbations.

### b. The governing equations

The model (Blumberg and Mellor 1983; Oey and Chen 1992, hereinafter referred to as OC) solves the finite-difference analog of the following set of equations assuming that the ocean is incompressible and hydrostatic, and using the Boussinesq approximation:

$$\nabla \cdot \mathbf{u} + \partial w / \partial z = 0 \quad (1a)$$

$$\begin{aligned} \partial \mathbf{u} / \partial t + \mathbf{u} \cdot \nabla \mathbf{u} + w \partial \mathbf{u} / \partial z + f \mathbf{k} \times \mathbf{u} \\ = -\nabla p / \rho_0 + \partial (K_M \partial \mathbf{u} / \partial z) / \partial z + \mathbf{F}_M \end{aligned} \quad (1b)$$

$$\rho g = -\partial p / \partial z \quad (1c)$$

$$\begin{aligned} \partial e / \partial t + \mathbf{u} \cdot \nabla e + w \partial e / \partial z \\ = \partial (K_H \partial e / \partial z) / \partial z + F_H \end{aligned} \quad (1d)$$

$$\rho = \rho(T, S, p). \quad (1e)$$

Here,  $\nabla$  is the horizontal gradient operator,  $\mathbf{u} = (u, v)$  is the horizontal velocity vector, and  $w$  is the vertical component of velocity;  $e$  denotes either the temperature  $T$  or salinity  $S$ , which are related to  $\rho$  through the equation of state (1e);  $f = 2\Omega \sin(\phi)$ , where  $\Omega = 7.292$

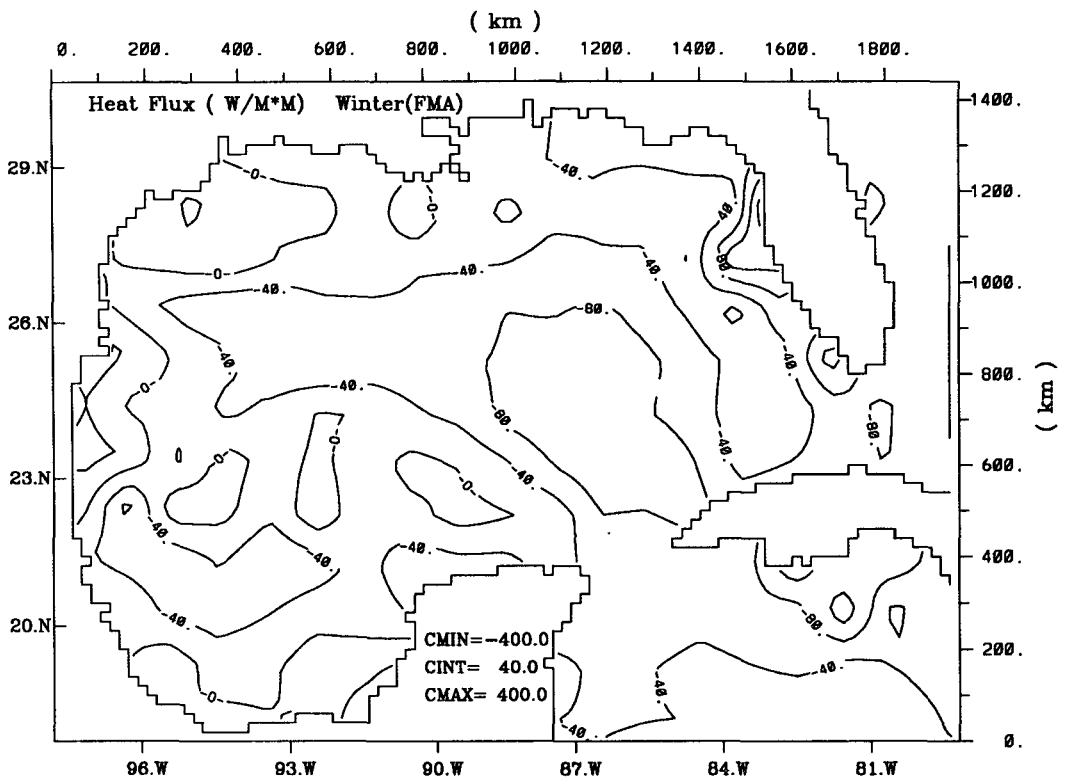


FIG. 2. Winter (average of Feb, Mar, and Apr; COADS) surface heat flux in watts per square meter used in the model. Plotted contours are mostly negative, indicating heat loss from ocean.

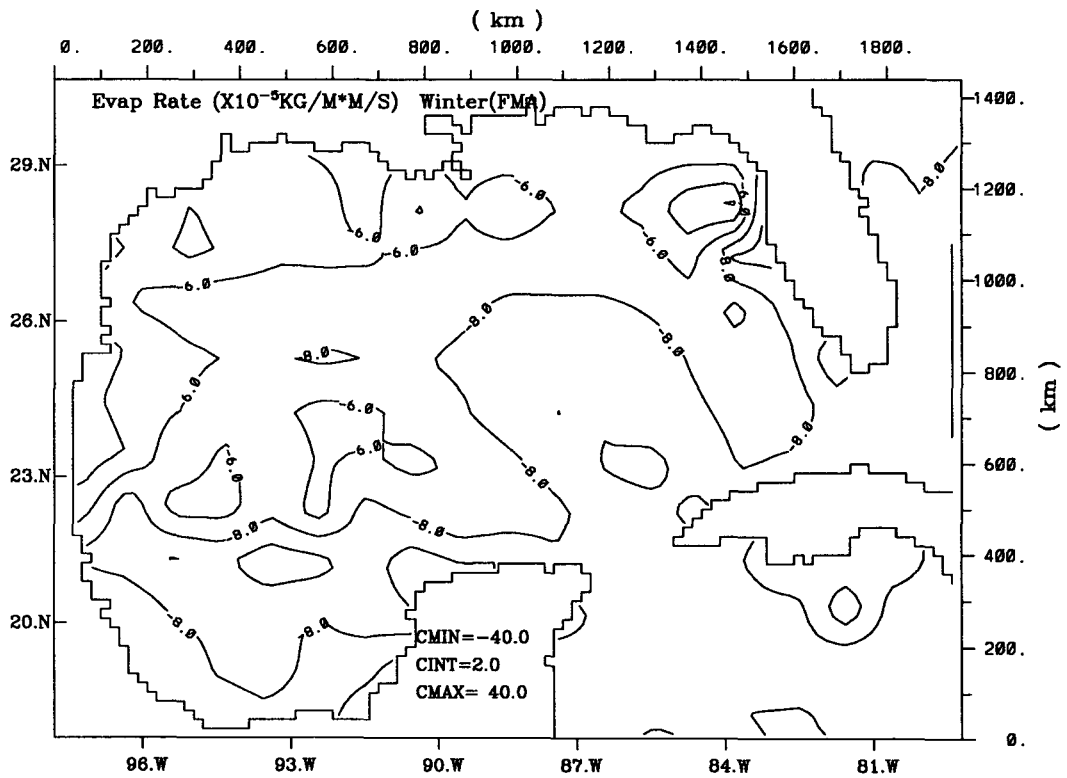


FIG. 3. Winter (average of Feb, Mar, and Apr; COADS) evaporative flux (in  $\text{kg m}^{-2} \text{ s}^{-1}$ ) used in the model. Plotted contours are mostly negative, indicating evaporation from ocean.

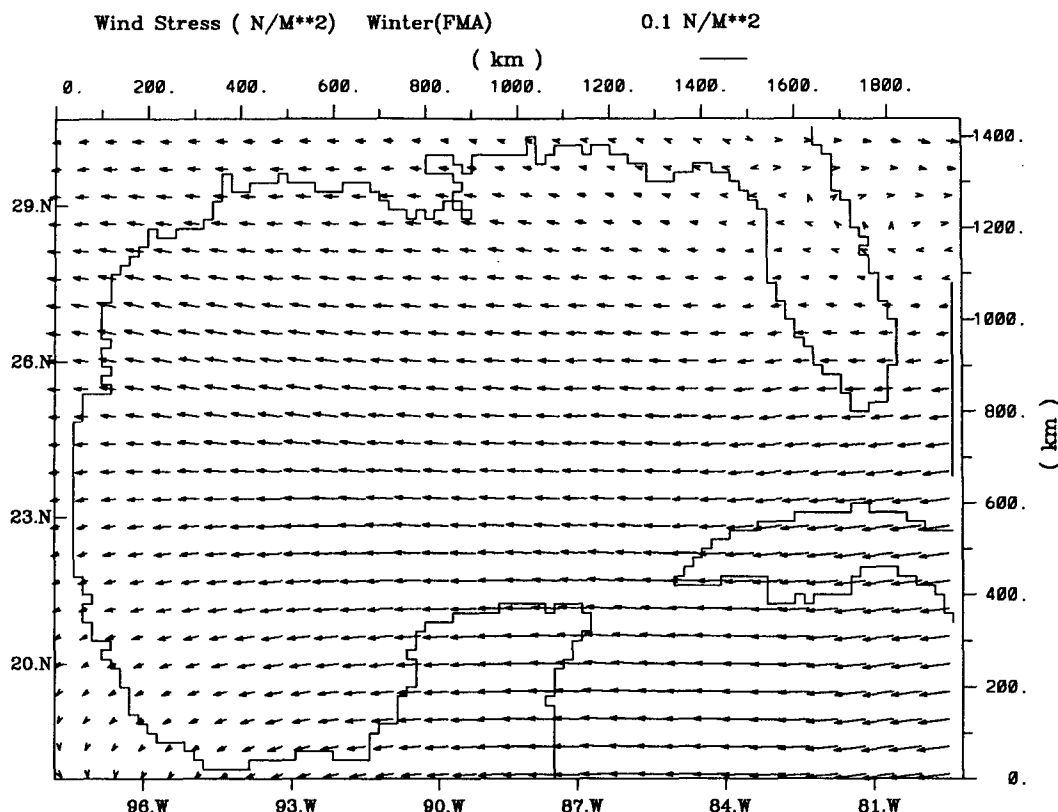


FIG. 4. Helleman and Rosentein's (1983) winter (average of Feb, Mar, and Apr) wind stress vectors used in the model.

$\times 10^{-5} \text{ s}^{-1}$  and  $\phi$  is the latitude. The equation of state is due to Mellor (1991). The  $F_M$  and  $F_H$  are Laplacian-type horizontal viscosity and diffusion terms, respectively, with coefficients  $A_M$  and  $A_H$  taken to be equal,

modeled by the Smagorinsky's (1963) diffusion formulation (OC):

$$A_M \text{ or } A_H = C \Delta x \Delta y [u_x^2 + v_y^2 + (u_y + v_x)^2/2]^{1/2}, \quad (2)$$

TABLE 1. Summary of model experiments.

Experiment	Smagorinsky's constant $C$	Integration time (days)	Comments
C0	0.2	240	120 days diagnostic, then 120 days prognostic initialization run for experiments C1, C3, C4, and C5; standard forcing <sup>a</sup>
C1	0.1	3645	Initialized from C0 with "C" linearly decreased to 0.1 over 10 days; standard forcing
C2	0.075	3630	First 30 days diagnostic, then 3600 days prognostic; standard forcing
C2A	0.075	3630	Same as C2 except that 30 Sv inflow was specified across the southwestern boundary of the Caribbean Sea
C2B	0.075	3630	Same as C2 except that 30 Sv inflow was specified across the eastern boundary of the Caribbean Sea
C3	0.05	3890	Initialized from C0 with "C" linearly decreased to 0.05 over 10 days; standard forcing
C4	0.03	5035	Initialized from C0 with "C" linearly decreased to 0.03 over 10 days; standard forcing
C5	0.01	1205	Initialized from C0 with "C" linearly decreased to 0.01 over 10 days; standard forcing

<sup>a</sup> Helleman and Rosenstein (1983) winter-mean wind; winter heat and evaporative fluxes;  $T$  and  $S$  at boundaries specified from Levitus (1982) winter values: 30 Sv into the Caribbean, distributed as 15 Sv across southwestern portion and 15 Sv across the eastern boundary; 1 Sv inflow through the Old Bahama Channel;  $2.36 \times 10^4 \text{ m}^3 \text{ s}^{-1}$  river discharge. See text for details.

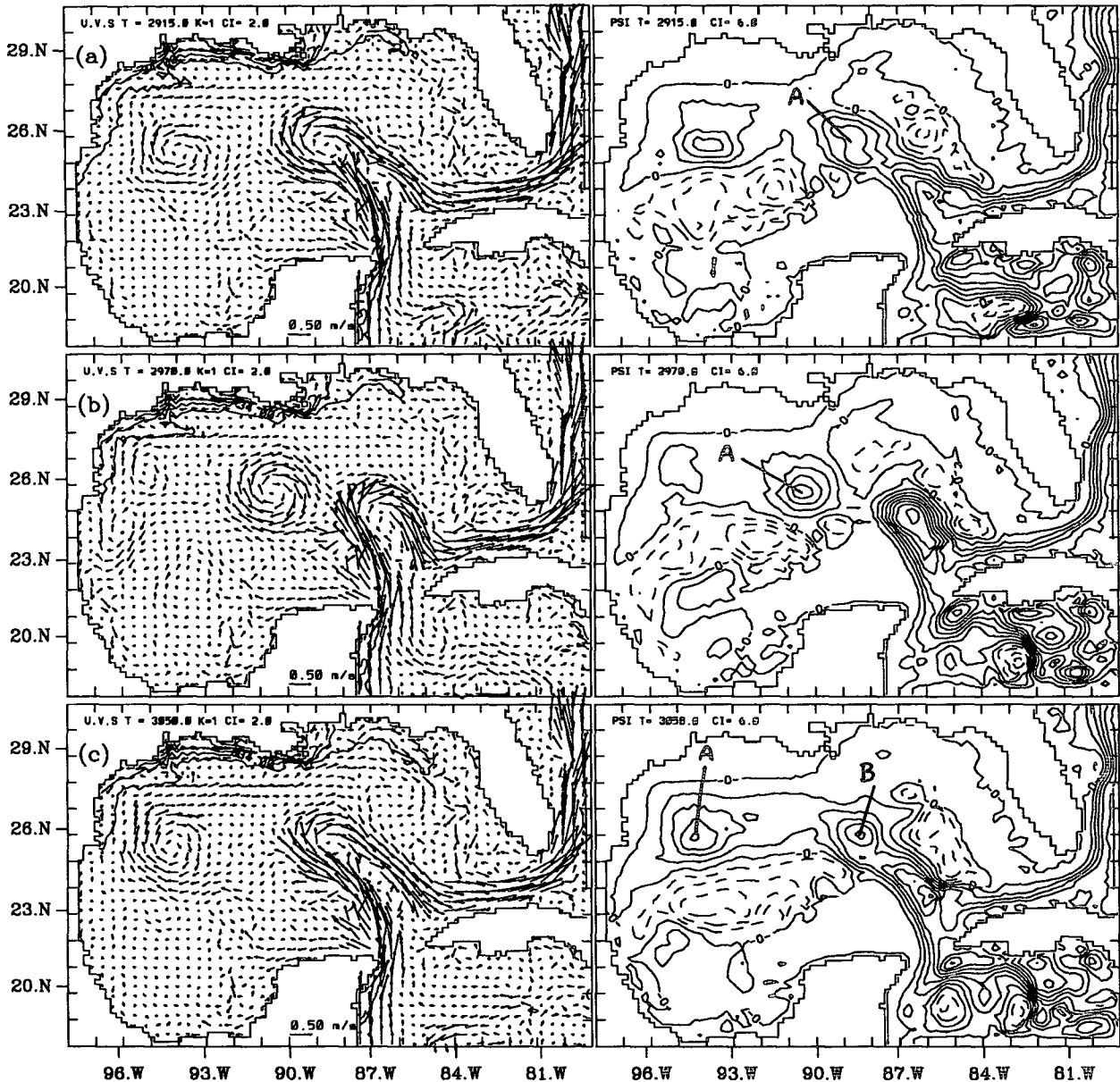


FIG. 5. Five-day averaged velocity vectors and LATEX shelf salinity (all at model sigma level 1; left panels) and streamfunction (right panels) for experiment C2 at time (a) 2915 days, (b) 2970 days, (c) 3050 days.

where  $C$  is a constant, which will be varied from 0.01 to 0.1 in the sensitivity experiments to be described below. The values of  $A_M$  ( $A_H$ ) range from 20 to 2000  $\text{m}^2 \text{s}^{-1}$  in the vicinity of the model LC. Vertical eddy viscosities and diffusivities,  $K_M$  and  $K_H$ , are calculated using the level-2.5 turbulence kinetic energy closure scheme of Mellor and Yamada (1982). We use constant grid sizes of  $\Delta x = \Delta y = 20$  km and 20 evenly distributed sigma layers in the vertical. The navy's DBDB-5 bottom topography is used, smoothed in the Caribbean with a Laplacian-type smoother. On the LATEX shelf, a linear depth variation from the 100-m iso-

bath on the outer shelf to the coast (with a minimum depth specified at 5 m) is used in place of the DBDB-5 depths. East of the Straits of Florida and some 300 km north of the South Bahama Channel, a meridional wall (free slip, see below) is used in place of the shallow shelf in that region. The model has a free surface, and for computational efficiency, time integration is split into a two-dimensional, external mode with a short time step of 40 seconds, and a three-dimensional internal mode with a long time-step of 20 minutes. For the domain shown in Fig. 1, the model requires about  $6.5 \times 10^6$  words of memory, about nine hours for a one-

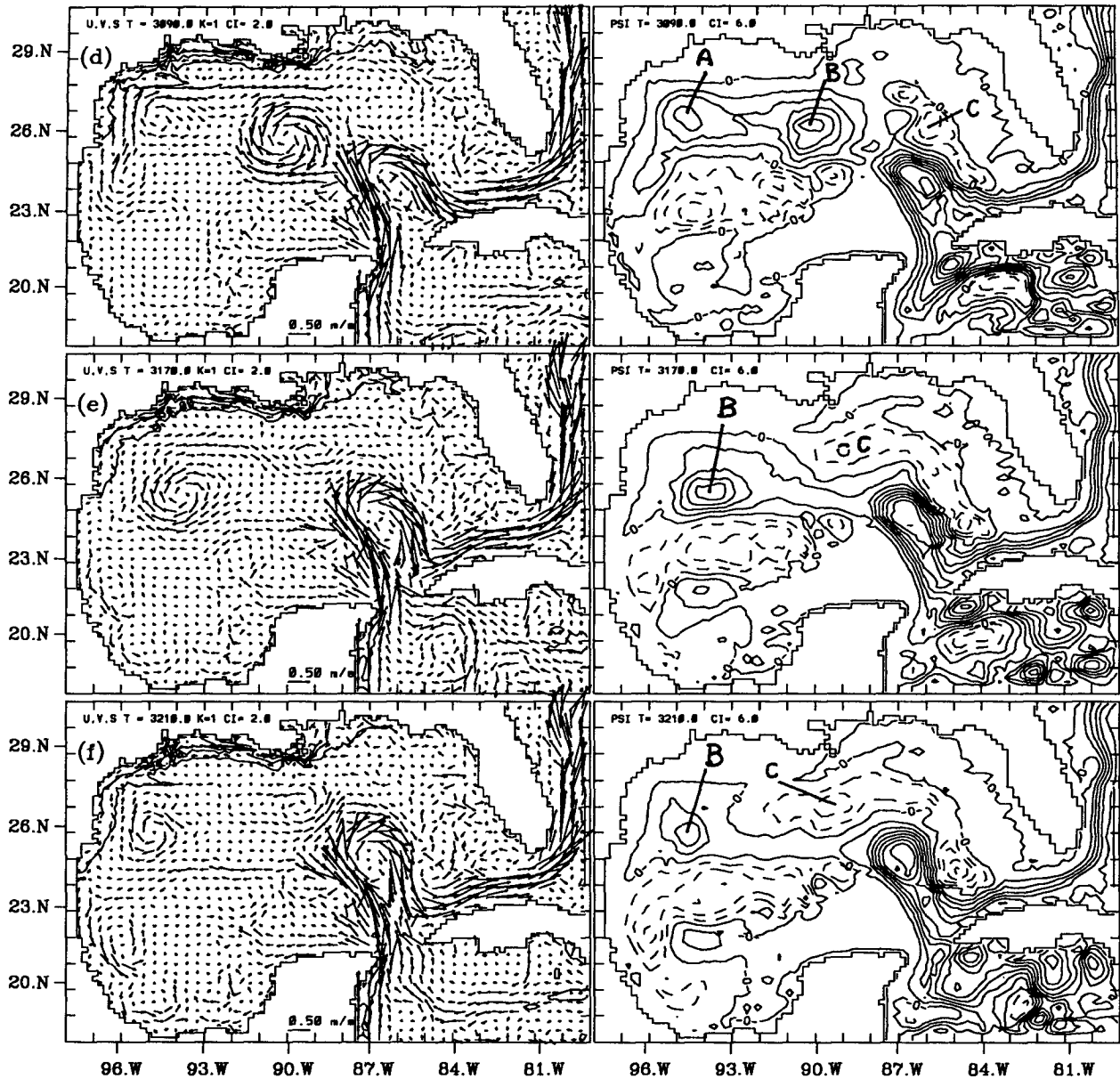


FIG. 5. (Continued) (d) 3090 days, (e) 3170 days, (f) 3210 days

year run on a Cray YMP, and achieves a high 195 Mflops rating.

### c. Boundary conditions

The normal velocities are zero at all side walls. In the C-grid system, which the model employs, the tangential velocities are also zero at a half-grid distance inside the walls, except in Straits of Florida where a free-slip condition is imposed. At the free surface,  $z \rightarrow \eta(x, y, t)$ :

$$K_M(\partial u/\partial z, \partial v/\partial z) = (\tau_0^x, \tau_0^y) \quad (3a)$$

$$K_H(\partial T/\partial z, \partial S/\partial z) = (T_{0s}, S_{0s}) \quad (3b)$$

$$w = \partial \eta / \partial t + \mathbf{u} \cdot \nabla \eta. \quad (3c)$$

Here  $\tau_0$  is the (kinematic) wind stress vector and

$$T_{0s} = -Q/(\rho_o C_{pw}) + C_1(T_{cs} - T) \quad (4a)$$

$$S_{0s} = S_s(E - P)/\rho_o + C_1(S_{cs} - S), \quad (4b)$$

where  $Q$  is the total heat flux in  $\text{W m}^{-2}$ , positive upward,  $C_{pw}$  the specific heat for water, taken from Gill (1982) to be  $4000 \text{ J kg}^{-1} \text{ K}^{-1}$ ,  $(E - P)$  is the net evaporation minus precipitation rate in  $\text{kg m}^{-2} \text{ s}^{-1}$ ,  $S_s$  is the surface salinity taken as being equal to the salinity

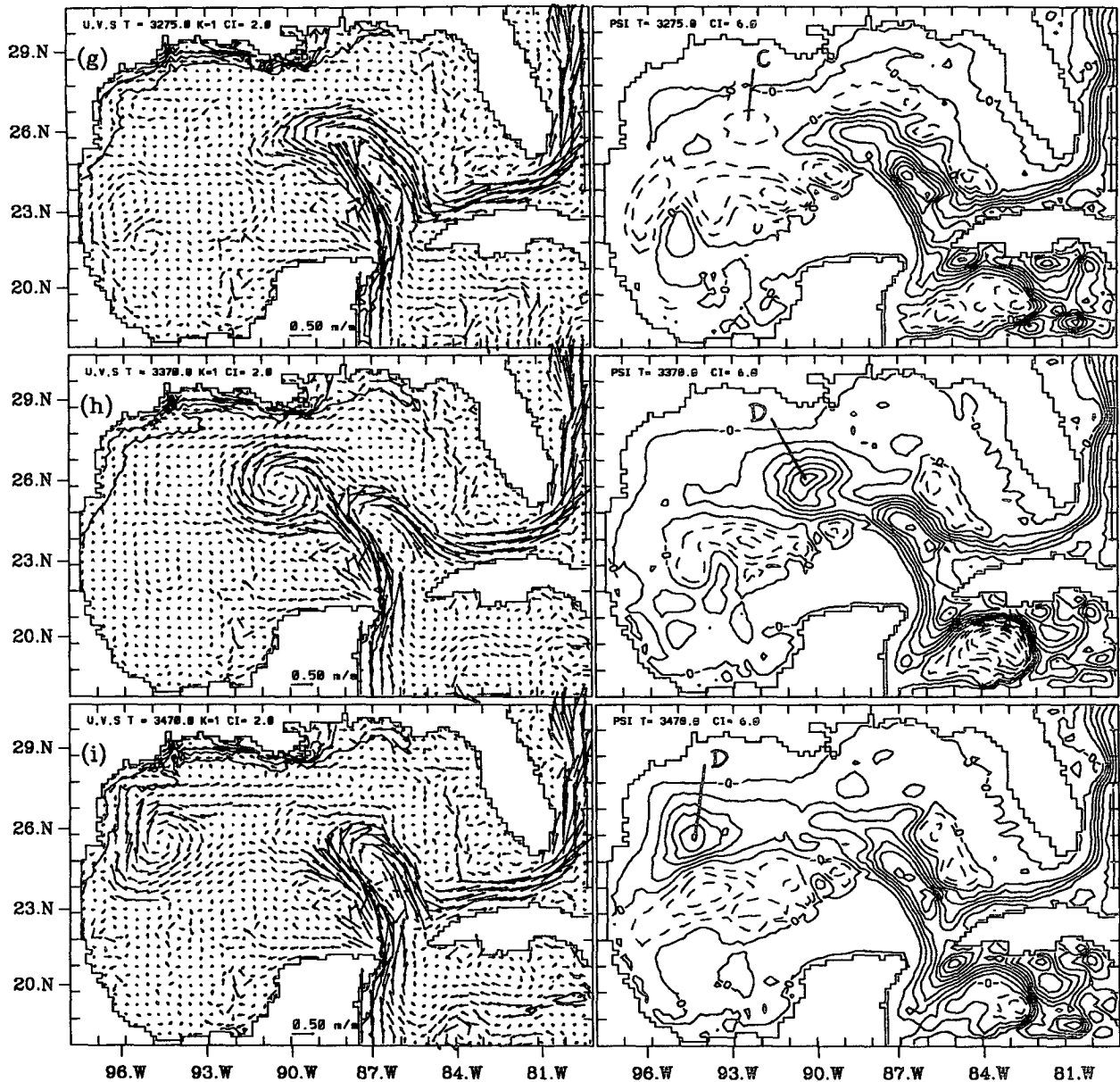


FIG. 5. (Continued) (g) 3275 days, (h) 3370 days, and (i) 3470 days.

at the first sigma level near the surface,  $T_{cs}$  and  $S_{cs}$  are climatological surface temperature and salinity, respectively, and  $C_1$  is a relaxation constant with unit in  $\text{m s}^{-1}$ . For small  $|Q|$  and  $(E - P)$ , and in the absence of fluxes due to other physical processes (e.g., advection or river discharge), the temperature and salinity in the upper  $h_1$  meters, say, of the ocean adjusts to their respective climatological values on a timescale of  $h_1/C_1$  seconds. The heat and evaporative fluxes (Figs. 2 and 3) correspond to wintertime conditions averaged from February through April and are from the Surface Marine Observation dataset (now COADS; courtesy of

J. Herring) of the National Climatic Data Center. Note that cooling is predominantly over the LC, and heat loss over the LATEX shelf is small. The wind stress averaged over the same period is taken from Hellerman and Rosenstein (1983) and is shown in Fig. 4. The reason for choosing a wintertime forcing is twofold, both stemming from considerations of future LATEX shelf simulations. First, winter cooling makes it convenient to use temperature as an indicator of cross-shelf contrast. Second, a wintertime model spinup would serve as a simpler initial condition in experiments to study the effects of seasonal

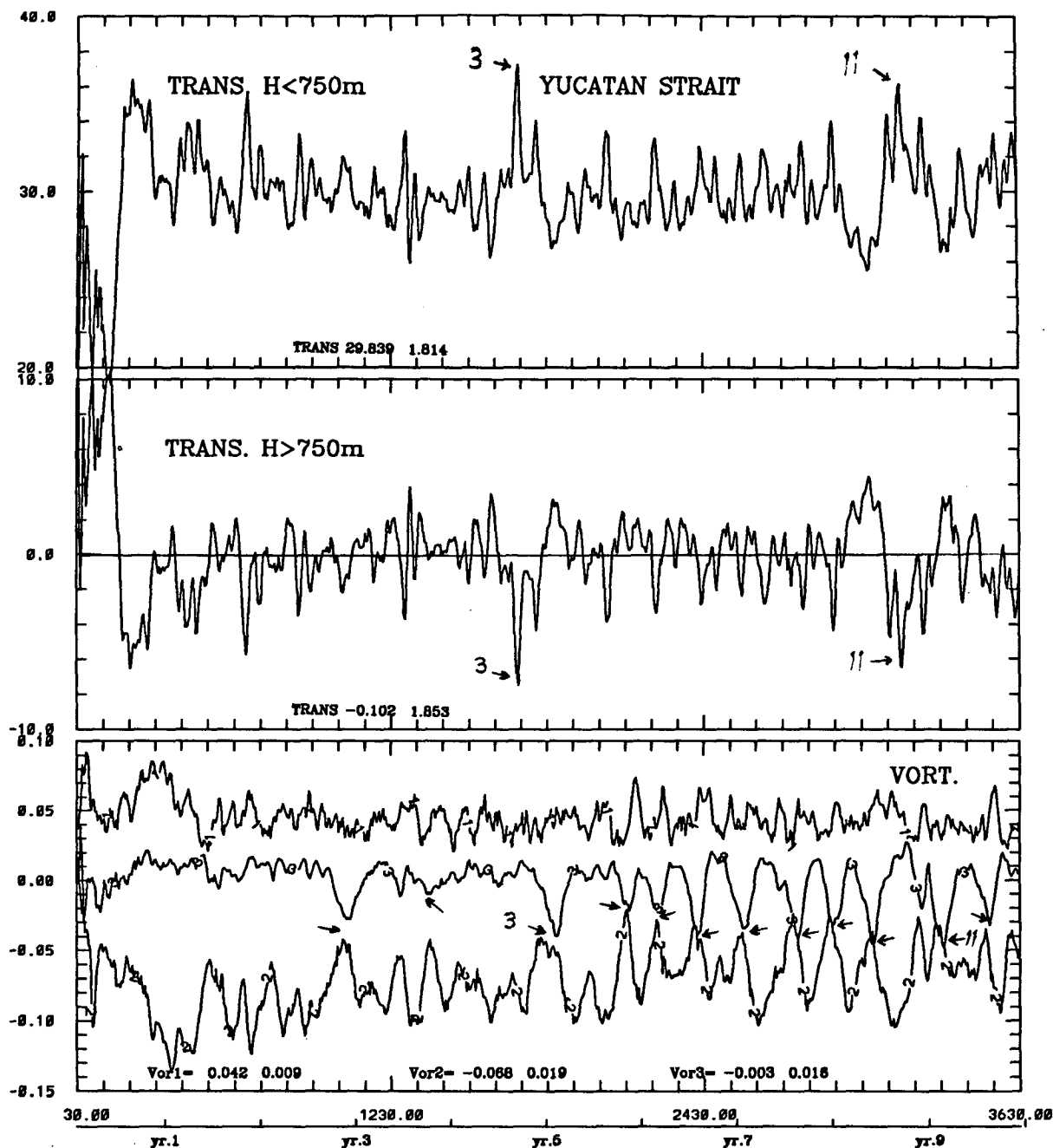


FIG. 6. (a) Time series of the upper (above 750 m, top panel) and lower-layer (below 750 m, middle panel) transports (Sv) in the Yucatan Channel (expt C2). The bottom panel shows area-averaged relative vorticities divided by the Coriolis parameter in regions 1, 2, and 3 (see Fig. 7). Arrows indicate eddy sheddings (3 and 11 are marked).

forcing on the shelf. To avoid excessive cooling at some semi-enclosed, coastal grid points where horizontal advective and diffusive processes are weak, a nonzero value of the relaxation constant  $C_1$  ( $=3.47 \times 10^{-7} \text{ m s}^{-1}$ ; relaxation time  $\sim 1$  year for the upper 10 m) is used. Some shorter ( $\sim 4$  years) experiments have been conducted to verify that the LC and LCE

sheddings are little affected by this nonzero value of the relaxation constant.

At the ocean floor,  $z = -H(x, y)$ , salt and heat fluxes are zero while momentum flux is balanced by matching the computed velocity,  $u_b$ , nearest the bottom  $z = z_b$  with the logarithmic law of the wall:



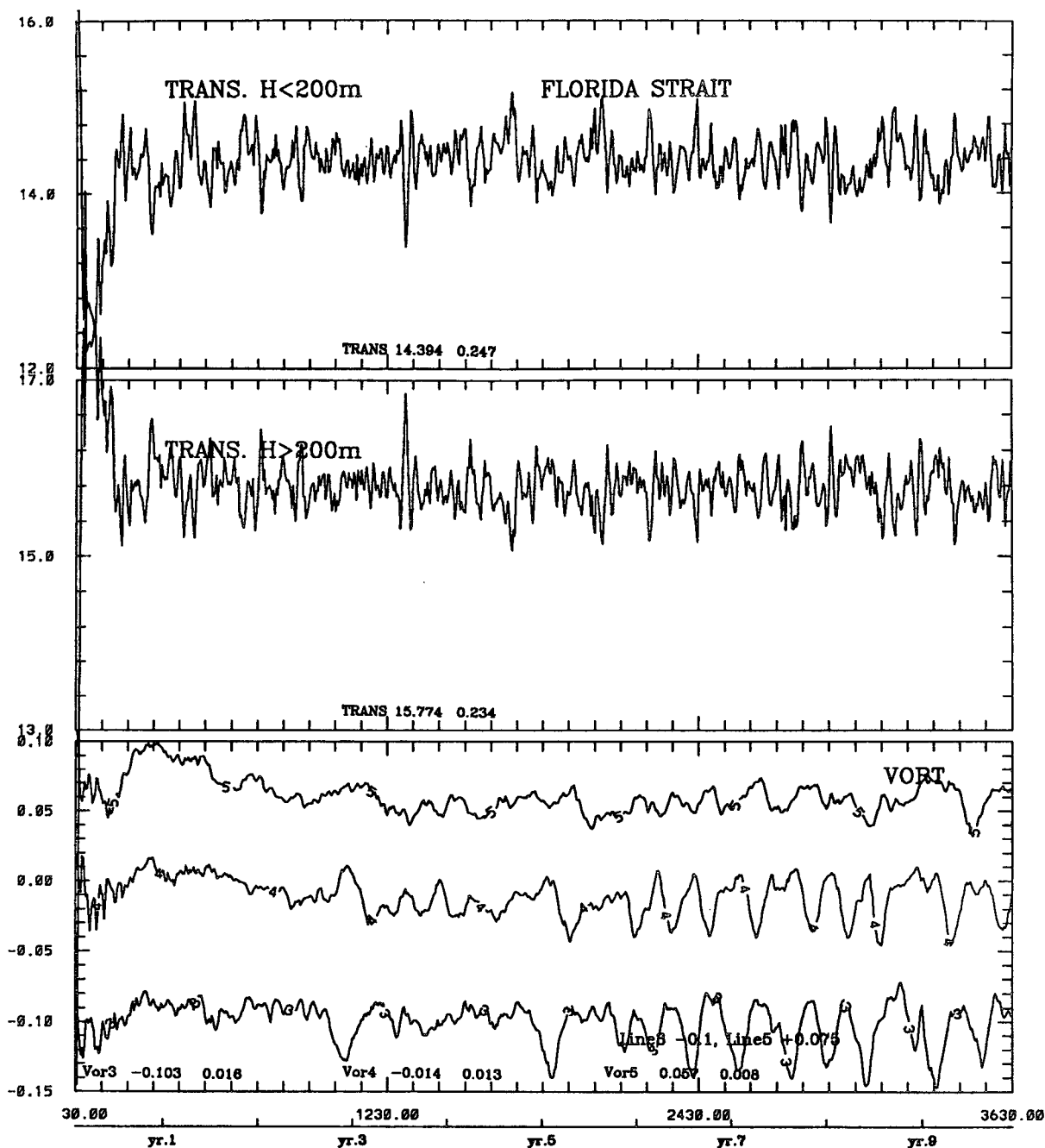


FIG. 6. (Continued) (b) Time series of the upper- (above 200 m, top panel) and lower-layer (below 200 m, middle panel) transports (Sv) in the Straits of Florida at 81°W (expt C2). The lower panel shows area-averaged relative vorticities divided by the Coriolis parameter in regions 3 (curve shifted down by 0.1), 4, and 5 (curve shifted up by 0.075) as indicated in Fig. 7. Values in each panel show mean and standard deviation.

$$K_M(\partial \mathbf{u} / \partial z) = C_D |\mathbf{u}_b| \mathbf{u}_b, \quad (5a)$$

where  $C_D = \max\{2.5 \times 10^{-3}, (k/\ln[(H + z_b)/z_r])^2\}$ ,  $k = 0.40$  is the von Kármán constant,  $H$  is local depth, and  $z_r = 0.005[1 + 1/H]$  m is the roughness height. The variable height is used to

simulate (in an ad hoc way; Mellor, personal communication 1988) increased roughness in shallow waters where wave breaking is prevalent. For the present simulation,  $C_D$  ranges from about  $2.7 \times 10^{-3}$  in shelfbreak regions where  $H \sim 200$  m, to about  $10^{-2}$  in shallow waters where  $H \sim 5$  m. In deeper

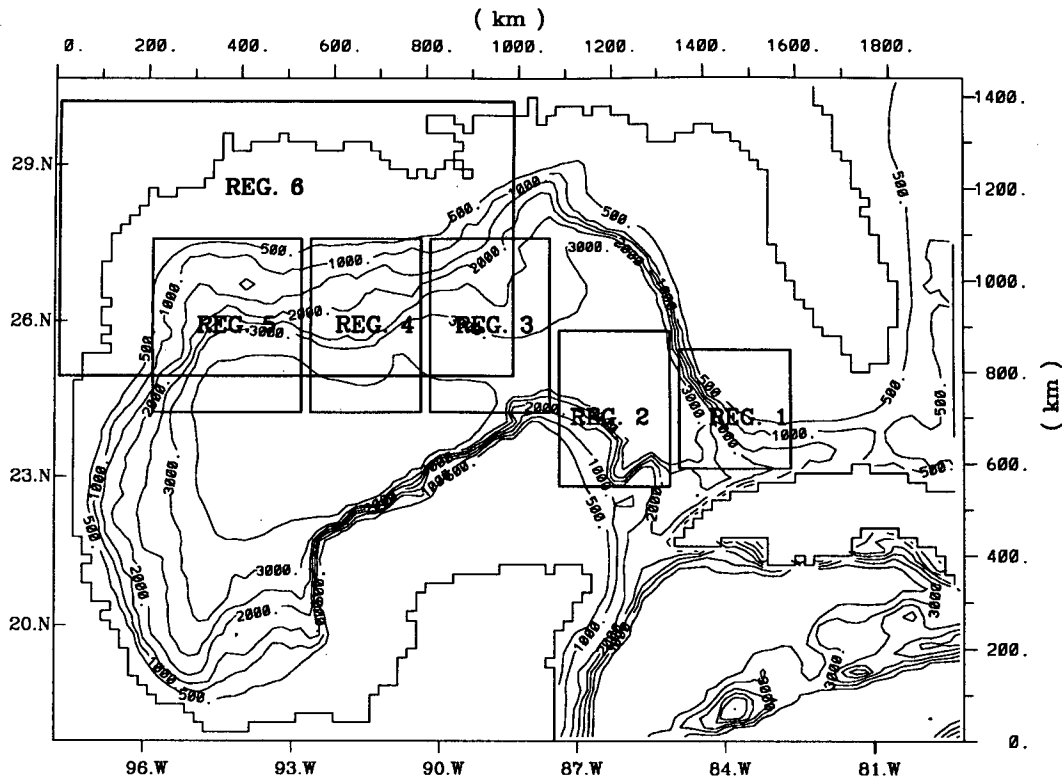


FIG. 7. Regions 1 through 6 where area-averaged vorticities are computed.

waters ( $H > 300$  m) where the logarithmic layer cannot be resolved,  $C_D = 2.5 \times 10^{-3}$ . Finally, the requirement that the ocean bottom is a material surface gives

$$w = -\mathbf{u} \cdot \nabla H. \quad (5b)$$

### 1) RIVER DISCHARGE

During high runoff, the combined discharge of the Mississippi and Atchafalaya Rivers is  $O(2 \times 10^4 \text{ m}^3 \text{ s}^{-1})$ , approximately two-thirds of which is from the Mississippi and one-third the Atchafalaya (Wiseman, personal communication 1993). The discharge from the Mississippi is through three main tributaries, the width of each is  $O(100 \text{ m})$ , and the width of the Atchafalaya River is approximately 300 m at its seaward end. The narrowness of these rivers, together with the high discharge, suggests a buoyant jet feature with two length scales: the width of river,  $L_q$ , and a buoyancy-related scale,  $L_b = M^{3/4}/B^{1/2}$ , where  $M = QU$ ,  $B = g'Q$ ,  $Q = L_q HU$  is the discharge rate,  $g' = g(\Delta\rho/\rho_0)$  is the reduced gravity,  $H$  is depth, and  $U$  is cross-sectionally averaged discharge velocity. Substituting typical values,  $L_b$  is about 10 to 20 m. Thus, for model grid sizes of 1 km or more, the precise configuration of the river mouth is irrelevant, and we assume that far-field (where distances  $\gg L_b$ ) effects of buoyancy can

be distributed over at least one grid area off the river mouth. The approximation can be expected to be more accurate as the model grid is refined to, say,  $O(1 \text{ km})$ ; it is not valid if further grid refinement is made, in which case explicit inclusion of the rivers is necessary (and, of course, becomes feasible).

We specify downward vertical velocities  $w_s = -Q/(N\Delta x\Delta y)$ , where  $N$  is the number of grid areas around the river mouth where the discharge is to be distributed, at the surface of three model grid points: one off the Mississippi River Delta, one at the mouth of the Atchafalaya River, and one at  $29^\circ 20' \text{ N}$ ,  $94^\circ 30' \text{ W}$  (Fig. 1; so that  $N = 1$  in each case). The last is to account for the combined discharge from the Sabine, Neches, Trinity, San Jacinto, Brazos, and San Bernard Rivers. We assume that these surface vertical velocities inject volumes and freshwaters ( $S = 0$  ppt) but no momentum. This requires rewriting the volume conservation equation in the external mode of the model as

$$\eta_t + \nabla \cdot (\mathbf{U}D) = w_s(x, y, t), \quad (6)$$

where  $D = H + \eta$  and  $\mathbf{U}$  is the depth-averaged velocity. The injected water must also be assigned a temperature,  $T_s$ , and this is taken to be equal to climatological values. The discharges, averaged over January, February, and March, are from Cochran and Kelly (1986), and are approximately  $15\,000$ ,  $7500$ , and  $1100 \text{ m}^3 \text{ s}^{-1}$  re-

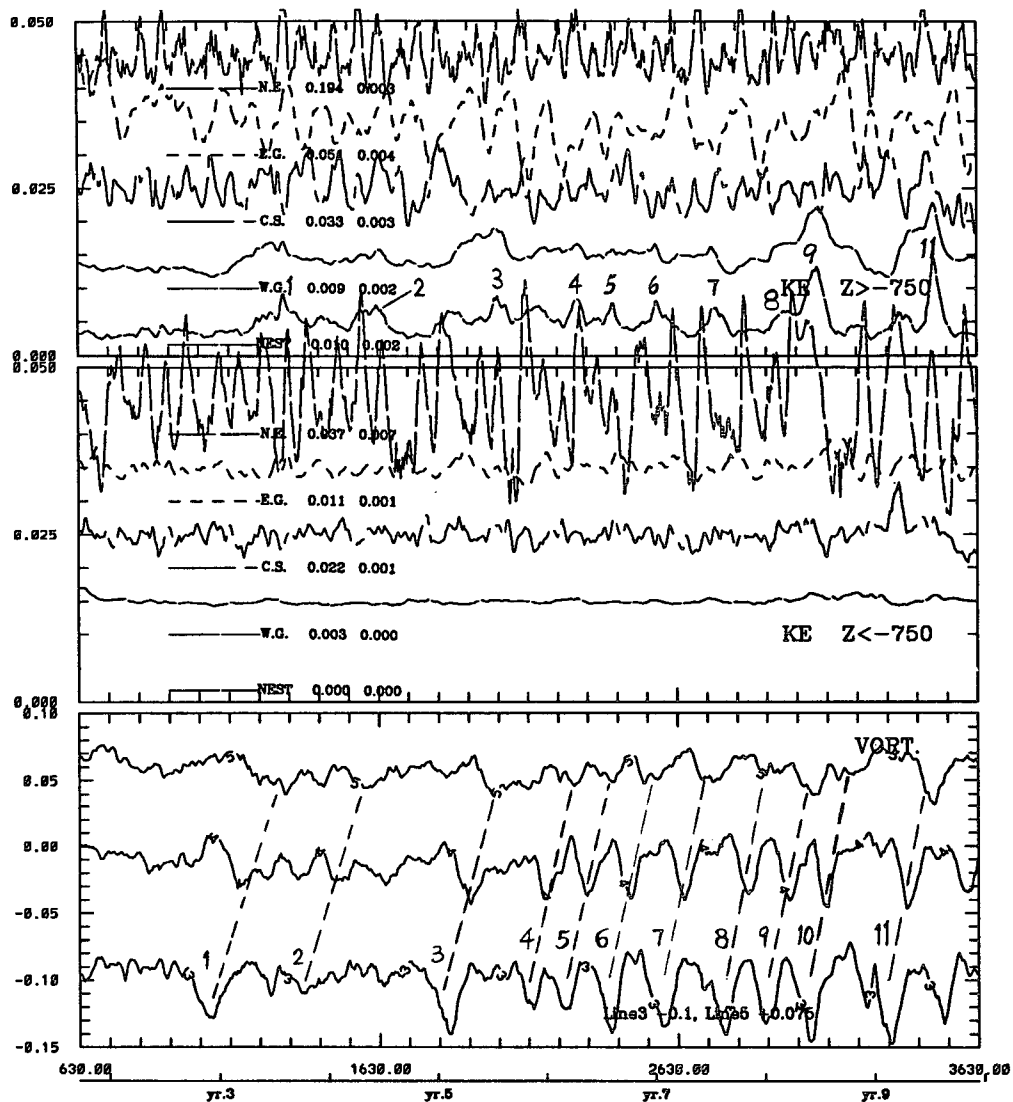


FIG. 8. Time series of the upper- (above 750 m, top panel) and lower-layer (below 750 m, middle panel) kinetic energies ( $\text{m}^2 \text{s}^{-2}$ ) for experiment C2, area-averaged over the five regions as indicated in Fig. 9. In the NEST region, average is over water depths less than 200 m. Only the last 3000 days are plotted, and means have been subtracted from the KE plots to show the fluctuation parts. The bottom panel shows area-averaged relative vorticities divided by the Coriolis parameter in regions 3 (curve shifted down by 0.1), 4, and 5 (curve shifted up by 0.075) as indicated in Fig. 7. Values in each panel show mean and standard deviation.

spectively for the three runoff grids. There is a one-month lag between discharge and the atmospheric forcing.

## 2) THE OPEN OCEAN BOUNDARY

We briefly describe the open boundary conditions (details in OC). Salinity and temperature are specified using the Levitus (1982) wintertime climatological values during inflow and advected out of the domain during outflow. In the Caribbean, a 30 Sv ( $\text{Sv} \equiv 10^6 \text{m}^3 \text{s}^{-1}$ ) inflow is specified, divided as 15 Sv across the

southwestern boundary (Fig. 1:  $18^\circ\text{N}$ ,  $86.5^\circ$ – $87.5^\circ\text{W}$ ) and 15 Sv across the eastern portion ( $18^\circ$ – $20.5^\circ\text{N}$ ,  $79^\circ\text{W}$ ). In two sensitivity experiments (see below), the 30-Sv inflow was specified either across the southwestern boundary, or across the eastern portion.

We also specify 1-Sv inflow through the Old Bahama Channel (Fig. 1:  $22.8^\circ$ – $23.8^\circ\text{N}$ ,  $79^\circ\text{W}$ ). All of these inflows, plus river discharges, are allowed to exit across the northeastern zonal boundary of the model domain in the South Atlantic Bight (Fig. 1:  $79^\circ$ – $80.2^\circ\text{W}$ ,  $30.7^\circ\text{N}$ ), seaward from the 400-m isobath. We assume zero transport across the northern zonal bound-

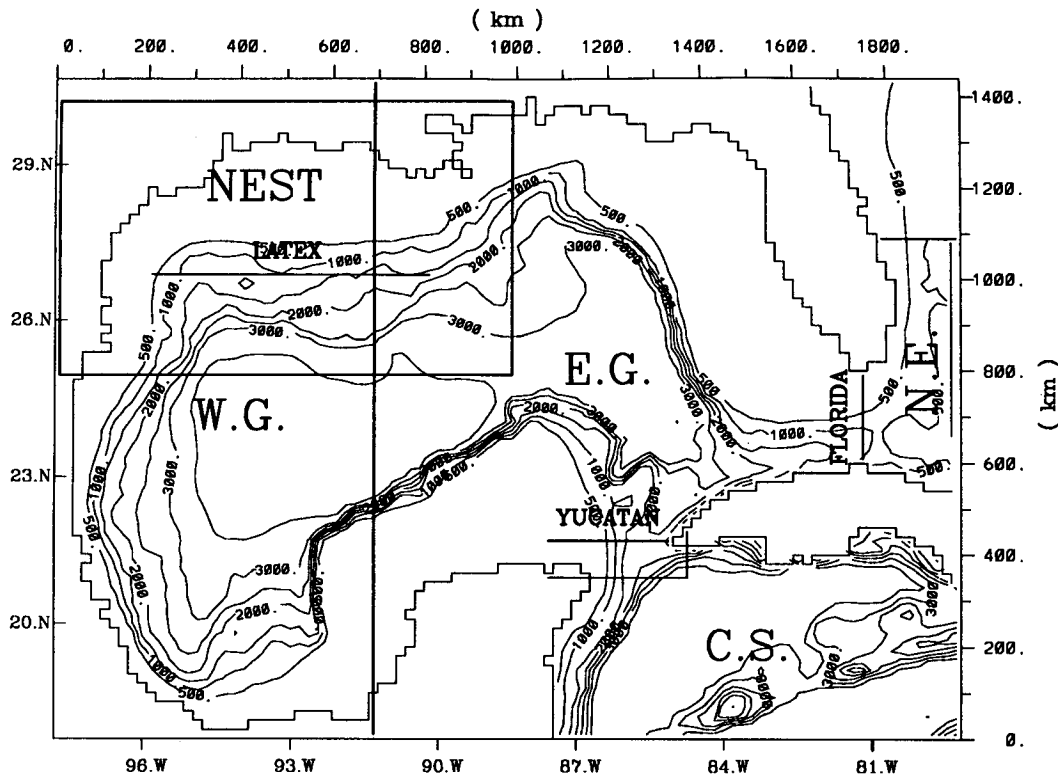


FIG. 9. Regions where area-averaged kinetic energies are computed.

ary on the shelf and also across the eastern meridional boundary in the South Atlantic Bight. A radiation condition is used for the 3D velocities normal to boundaries with a constant internal phase speed equal to  $(Hg \times 10^{-3})^{1/2}$ , and tangential velocities are advected with zero values used during inflow (OC). Free-slip condition is applied along the entire meridional boundary in the Straits of Florida north of 24.5°N to overcome excessive accumulation of vorticity near the northeast corner. We have found that the modeled LC and LCEs (times of shedding, eddy sizes, etc.) are not sensitive to the exact form of the outflow conditions.

#### d. Initial conditions

The calculation was initialized with the Levitus (1982) wintertime climatology (not shown). The Loop Current is barely discernable in the climatological fields, and the salinity field on the LATEX shelf resembles little of the pattern seen in the more detailed salinity maps given in Cochran and Kelly (1986). One of the first requirements of the model calculation is to correct these unrealistic features: that is, sharpening up gradients in the Loop Current and also in coastal areas.

### 3. Results

We conducted two sets of experiments (Table 1). The first set (experiments C1, C3, C4, and C5) was

initialized from a smooth 240-day “startup” run C0. The second set (experiments C2, C2A, and C2B) was initialized from a 30-day diagnostic run, so that one may estimate the spinup time required for the system to achieve a quasi-equilibrium state when eddies are shed. It turns out that the first eddy is shed in about 3 years, irrespective of the initialization process. All experiments differ in the value of the Smagorinsky constant  $C$ , except for C2A and C2B, which test different inflow conditions. Except for C5 (and other short-duration experiments that tested open boundary conditions and surface relaxation; see previous section), all experiments were conducted for 10 years or more.

#### a. LCE-shedding characteristics and dynamics

The LCE shedding sequence for experiment C2 (Fig. 5) is typical of other experiments, and is presented to illustrate (below) the interplay between shedding, LC, and transport in the Yucatan Channel. The modeled eddy dimensions of 300–400 km, westward propagation speeds of 4–5 km day<sup>-1</sup>, shedding periods of 170 days (from Fig. 5a to 5d) to 280 days (from Fig. 5d to 5h) are fairly realistic in view of observations (e.g., Elliot 1982). The aperiodicity of shedding, even after 8 years of integration, is in contrast to HT’s “standard” results with  $A_M = A_H = 10^3 \text{ m}^2 \text{ s}^{-1}$ . After spinups of 1–3 years, HT obtained eddy shedding with constant

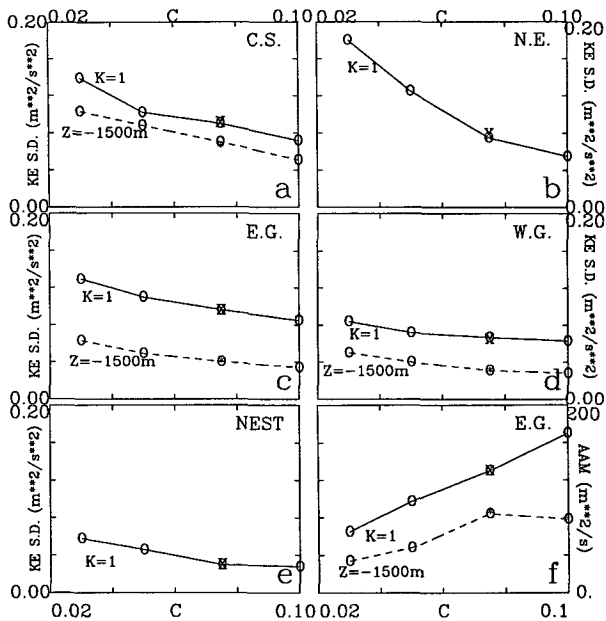


FIG. 10. (a)–(e) The standard deviation of kinetic energy at model sigma level 1 and  $z = -1500$  m averaged over the five regions as indicated in Fig. 9, as functions of the Smagorinsky constant  $C$ . The lowest right-hand panel (f) shows the horizontal viscosity in region E.G. Values were derived from seven or more years of calculations, excluding initial spinups.

periods of about 350 days in the reduced-gravity case and about 160 days (flat bottom) and 265 days (with topography) for a two-layer model. With reduced  $A_M$  and  $A_H$ , HT found aperiodic shedding, at least for the reduced-gravity case. For experiment C2, the  $A_M$  (or  $A_H$ ) is about  $100 \text{ m}^2 \text{ s}^{-1}$  in the main LC region. Thus, the modeled shedding irregularity appears to be a result of chaotic dynamics caused by reduced dissipation. Observations (e.g., Elliot 1982) also show irregular eddy sheddings, with periods that range from 5 to 18 months (average  $\sim 9$  mo).

When newly shed (Figs. 5b, 5d, and 5h), the maximum swirl transports (value of streamfunction at eddy's center) are 24 Sv (eddy A; Fig. 5b), 30 Sv (eddy B; Fig. 5d), and 36 Sv (eddy D; Fig. 5h); the latter being 6 Sv in excess of the total transport (30 Sv) specified across the model boundaries in the Caribbean. These eddies display a mix between a purely barotropic process in which the "upper layer" (that above the main thermocline,  $z > -750$  m, say) loses little energy to the bottom layer, resulting in intense LCEs (Fig. 5h), and a process with intense upper-to-lower layer transfer of energy through baroclinic instability, resulting in weaker eddies (Fig. 5b). Hurlburt and Thompson had demonstrated this latter process by using a two-layer model with a flat bottom, for which maximum energy transfer occurs. In general, our simulated swirl transports are less than 30 Sv, and upper-

to-lower layer energy transfers are prevalent. This too is to be expected from HT's two-layer calculation with topography.

Associated with each eddy shedding, reversed bottom flow occurs in the Yucatan Channel, as can be inferred from the cyclonic streamfunction (dashed) in the western portion of the model Caribbean (Figs. 5a,c, and h). The reversal or weakened northward flow at times extends to the surface layers along the eastern portion of the Channel (Figs. 5c,d, and h). In HT's two-layer model experiments with topography, eddy shedding ceased when the lower-layer ( $z < -H_1$ ) transport,  $Tr_2$ , was increased from 0 to 10 Sv (positive being inflow into the Gulf), the upper-layer transport,  $Tr_1$ , being fixed at 25 Sv. Regular eddy shedding was found for their standard experiment with  $Tr_2 = 5$  Sv. Thus increased  $Tr_2$  inhibits shedding, as shown by HT in terms of cessation of upper-layer deepening caused by near-zero divergence in the vicinity of the LC. For the present simulation, ten-year averaged  $Tr_1$  for experiment C2 is 13 Sv, and  $Tr_2 = 17$  Sv, with a standard deviation of about 1 Sv for both layers. If  $H_1$  is (more realistically) taken to be 750 m, which corresponds to approximately the thickness of the simulated LC, and transport time series in each layer is plotted (Fig. 6), a dynamical picture more in accord with HT's theory emerges. Now the averaged  $Tr_1$  con-

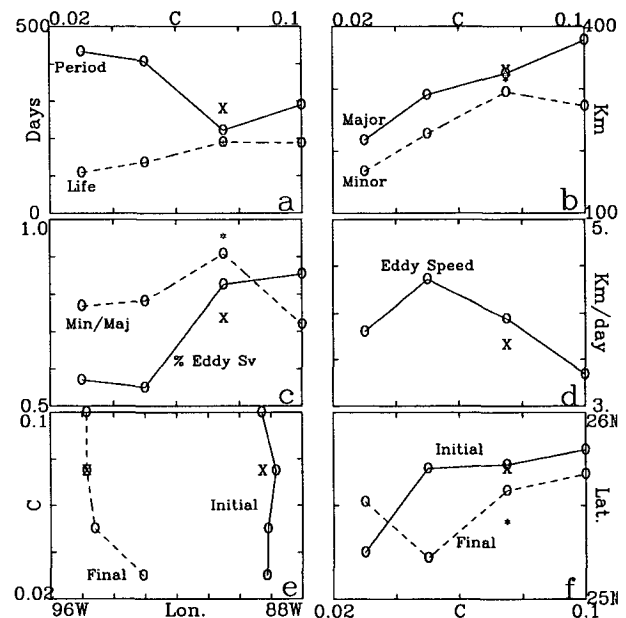


FIG. 11. Various modeled LCE characteristics as functions of the Smagorinsky constant " $C$ ": (a) shed period and eddy life, (b) major and minor eddy axes, (c) ratio of eddy swirl transport to 30 Sv, and minor/major axes ratio, (d) eddy westward propagation speed, (e) initial and final longitudes of eddy centers, and (f) initial and final latitudes of eddy centers. The stars and crosses are for experiment C2A. Values were derived from seven or more years of calculations, excluding initial spinups.

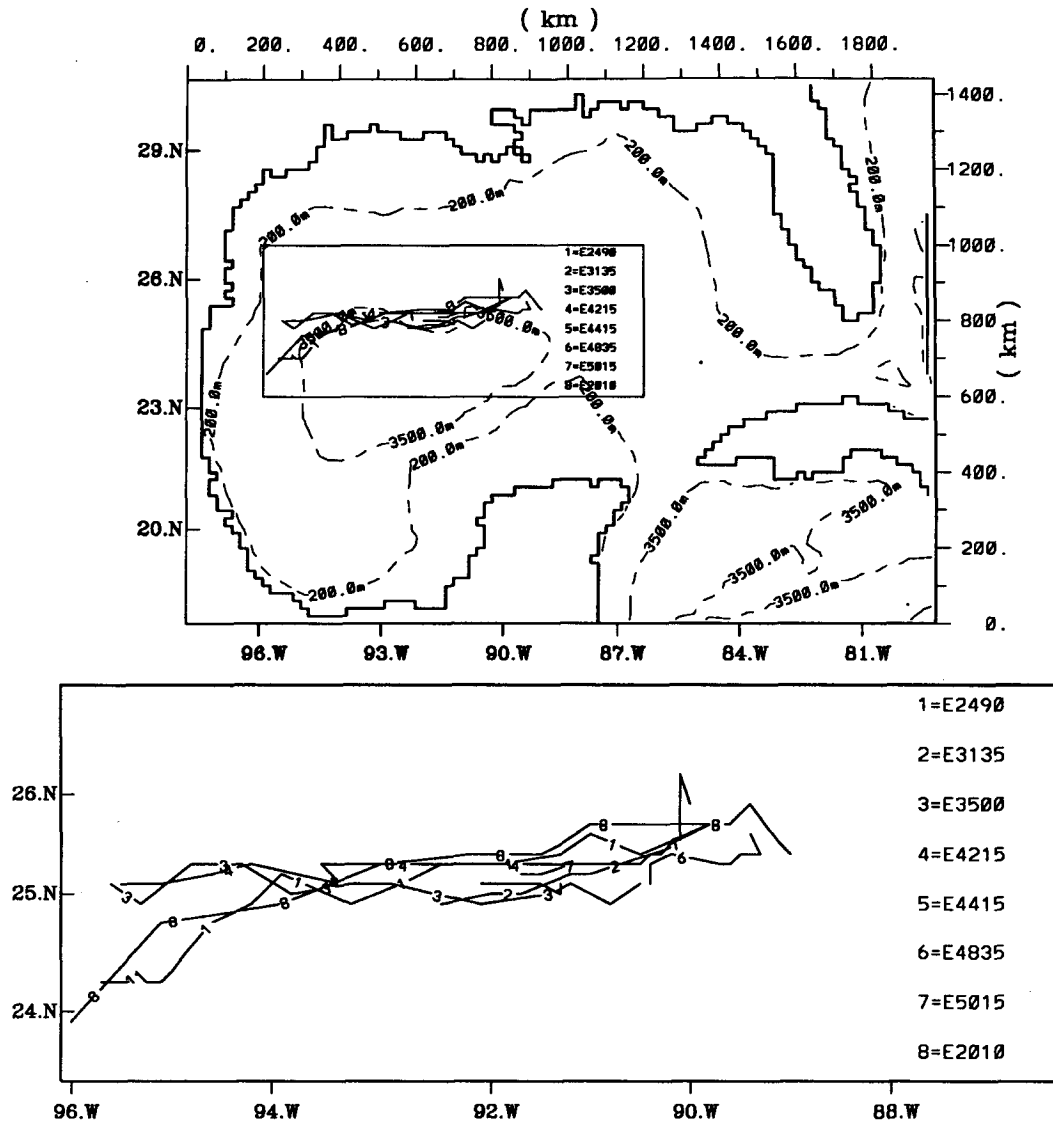


FIG. 12. Paths of eddy centers for experiment C4.

tains all of the 30 Sv that is specified (actually, if the first year or so of the transient is excluded, the averaged  $Tr_1 \approx 31$  Sv and  $Tr_2 \approx -1$  Sv), and the standard deviation is about 2 Sv. The upper- and lower-layer transports are anticorrelated; a decrease in one results in an increase in the other so that the total is constant at 30 Sv. When an eddy is shed, vorticity in region 2 (lower panel, curve 2, Fig. 6a, Fig. 7) increases (i.e., more positive or cyclonic), while that in region 3 decreases, with a time lag of about 1 mo or less. Eddy shedding begins at  $t = 1070$  days (about yr 3; cf. HT's two-layer model with topography), for a total of 12 eddies for this experiment. The period of shedding appears to become more regular after the fourth eddy (yr 6), with values which range from 150 to 280 days. Though the channel transports appear to fluctuate at higher frequen-

cies, correlation between shedding events and reversed bottom flow can be identified (e.g., events 3 and 11). The bottom reversed flows last from a few weeks to as long as 6 months (event 11) and in general precede sheddings, though this needs to be confirmed with more realizations. The evidence for the two processes to be related is overwhelming. In analyzing the near-bottom current meter time series in the Yucatan Channel, Maul et al. (1985; see also Burkov et al. 1982) noted prolonged (weeks to months) southward flow, which appeared to correlate with eddy shedding inferred from satellite imagery. The present model results support Maul's hypothesis of a return flow when an eddy sheds, but more observations are required to confirm it. This phenomenon does point out the importance of letting the Yucatan Channel boundary free, as was done here.

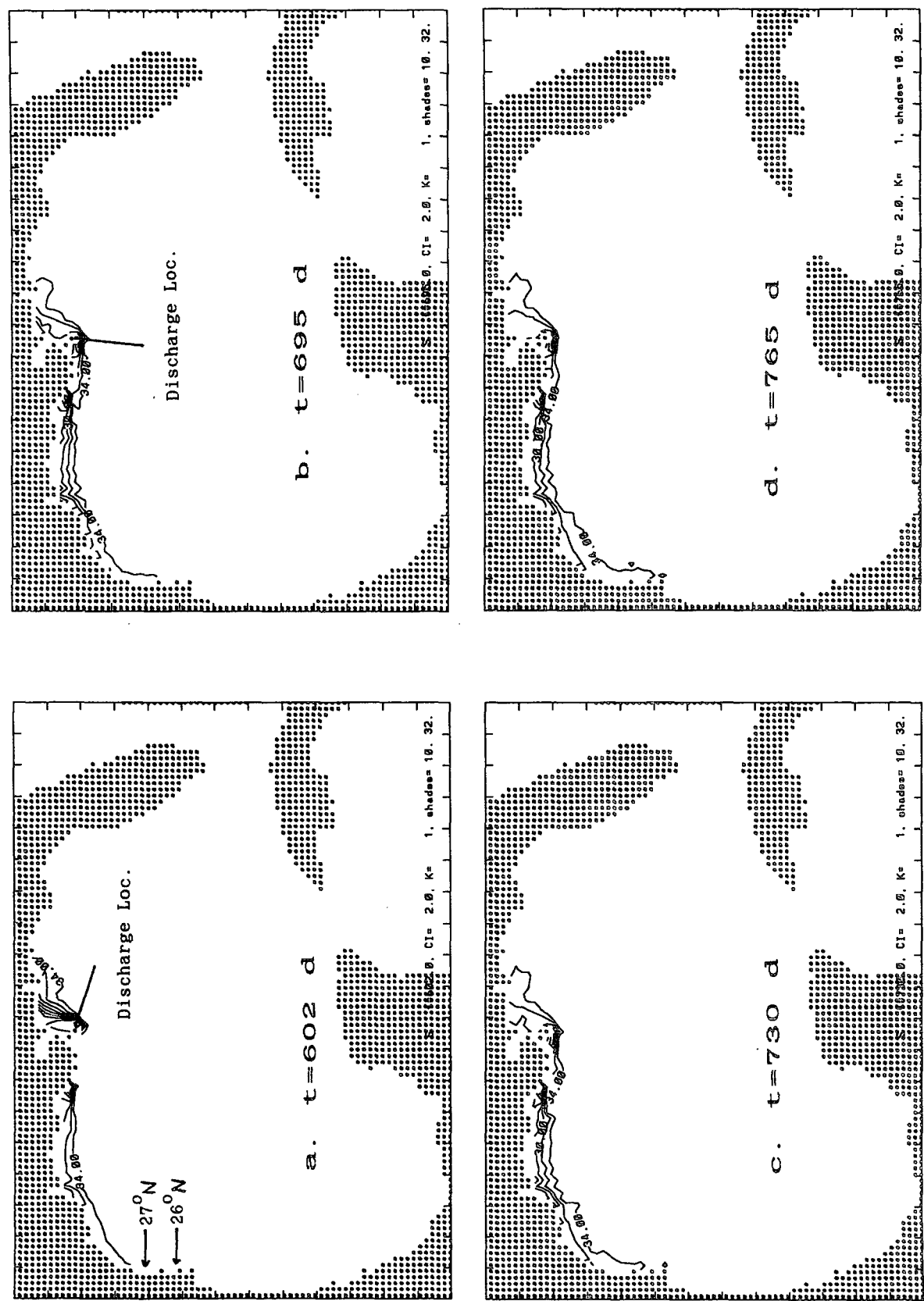


FIG. 13. Salinity at model sigma level 1 taken from the spinup phase of experiment C2 showing its sensitivity on the LATEX shelf to two different Mississippi River discharge locations (a) prior to  $t = 632$  days, and (b) (location "a" shifted southwestward) thereafter.





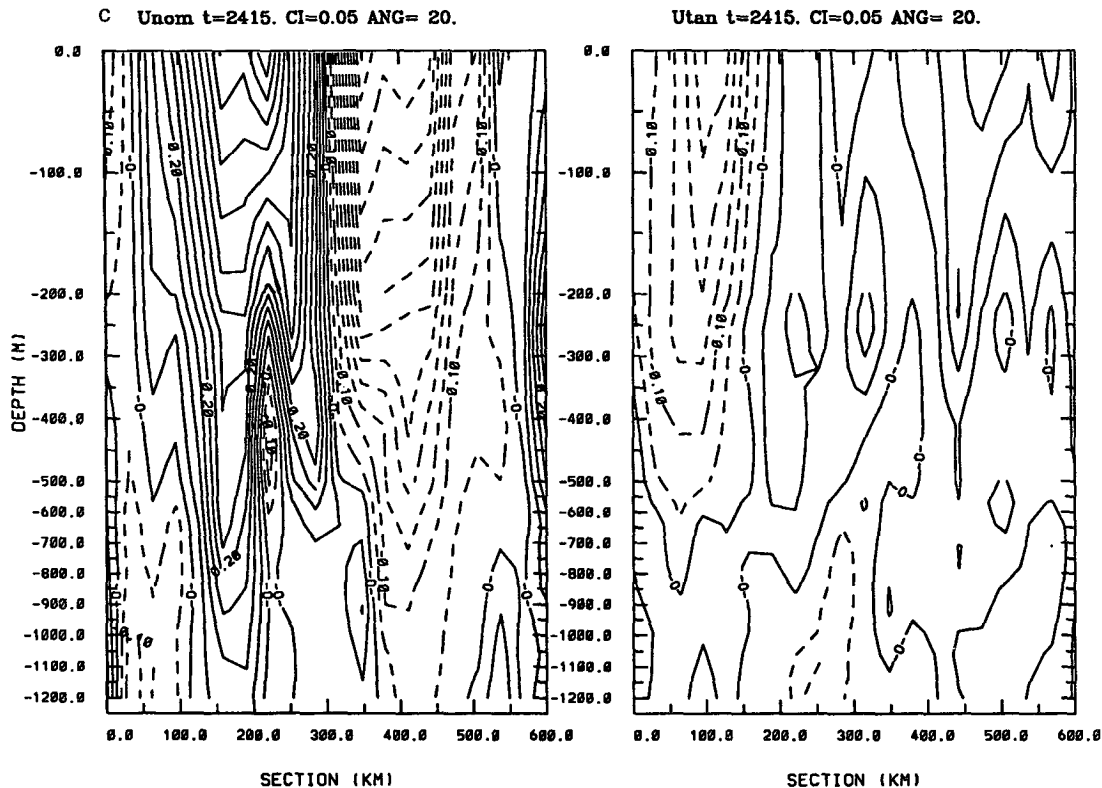


FIG. 14. (Continued)

Unlike the Yucatan Channel transport, that in the Straits of Florida shows no clear correlation with eddy shedding (Fig. 6b). There are short-period [ $O$  (weeks)] fluctuations (that are absent from the Yucatan Channel time series), and it is difficult to discern any correlation with the vorticity plots.

Since other forcing is steady, the variability in Fig. 5 is caused by the LC and eddies. Besides anticyclones, there are regions of cyclonic recirculation (off the West Florida slope) and eddies (e.g., eddy C in Figs. 5d–g). With each shedding, a cyclone “cuts” across the LC in the vicinity of  $26^{\circ}\text{N}$ ,  $87^{\circ}\text{W}$  (Fig. 5a for eddy A, 5c for eddy B, and 5g,h for eddy D). The development of cyclones off the West Florida slope prior to LCE sheddings can be seen in satellite images (Vukovich et al. 1979). However, the modeled LC tends to shed eddies farther north than observed.

Eddy-induced variability is shown in Fig. 8 for different parts of the Gulf in terms of kinetic energy (KE) and vorticity time series. Correlation is seen between the upper-layer KE fluctuations in the western Gulf/LATEX shelf and LCE arrivals and passages, as the numberings indicate. For events “9” and “11,” current fluctuations on the shelf are as large as  $\pm 0.1 \text{ m s}^{-1}$ . Higher-frequency fluctuations exist in the eastern Gulf (EG) and Caribbean Sea, associated with LC variabilities, not all of which result in LCE sheddings. Even

higher-frequency fluctuations (periods as short as weeks) appear in the Straits of Florida (NE); they are especially intense in the lower layers and are apparently unrelated to LC variabilities, as was also noted before in Fig. 6b. In the Caribbean, the KE is comparable to those in EG and NE especially in the lower layer, where it is actually larger than EG, consistent with the near-bottom reversed flow features explained previously in conjunction with Fig. 5.

#### b. Sensitivity to horizontal diffusivity and viscosity

In general, the eddy kinetic energy (EKE) is larger for smaller values of the Smagorinsky constant “ $C$ ” of the horizontal diffusivity and viscosity coefficients (Figs. 9 and 10). The variation is caused by fluctuations of small-scale eddies ( $< 100 \text{ km}$ ; see below) at smaller “ $C$ .” Similar inference is obtained for other variances. As “ $C$ ” is decreased, area-averaged  $\eta' \approx 2$  to  $6 \text{ cm}$  ( $\approx 2 \text{ cm}$  on LATEX),  $S' \approx 0.2$  to  $1 \text{ ppt}$  (LATEX), and  $T' \approx 0.5$  to  $1^{\circ}\text{C}$ . The large  $S$  and  $T$  variances over the LATEX shelf are caused primarily by eddy impingement on the northwestern Gulf (Oey 1995).

To assess LCE characteristics as functions of “ $C$ ,” we calculated for each experiment the LCE shedding periods, eddy life spans, maximum major

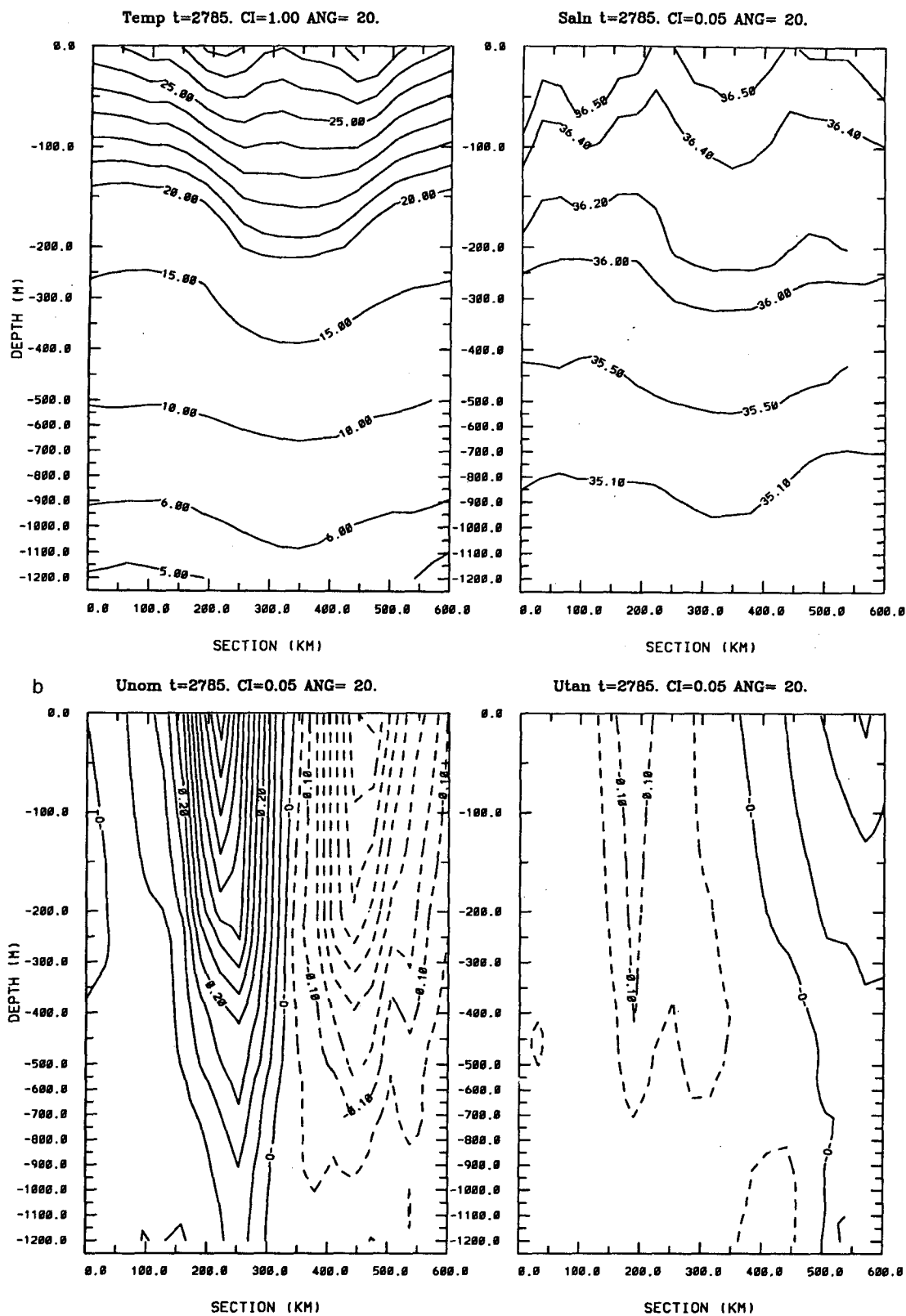


FIG. 15. As in Fig. 14b,c but for experiment C1.

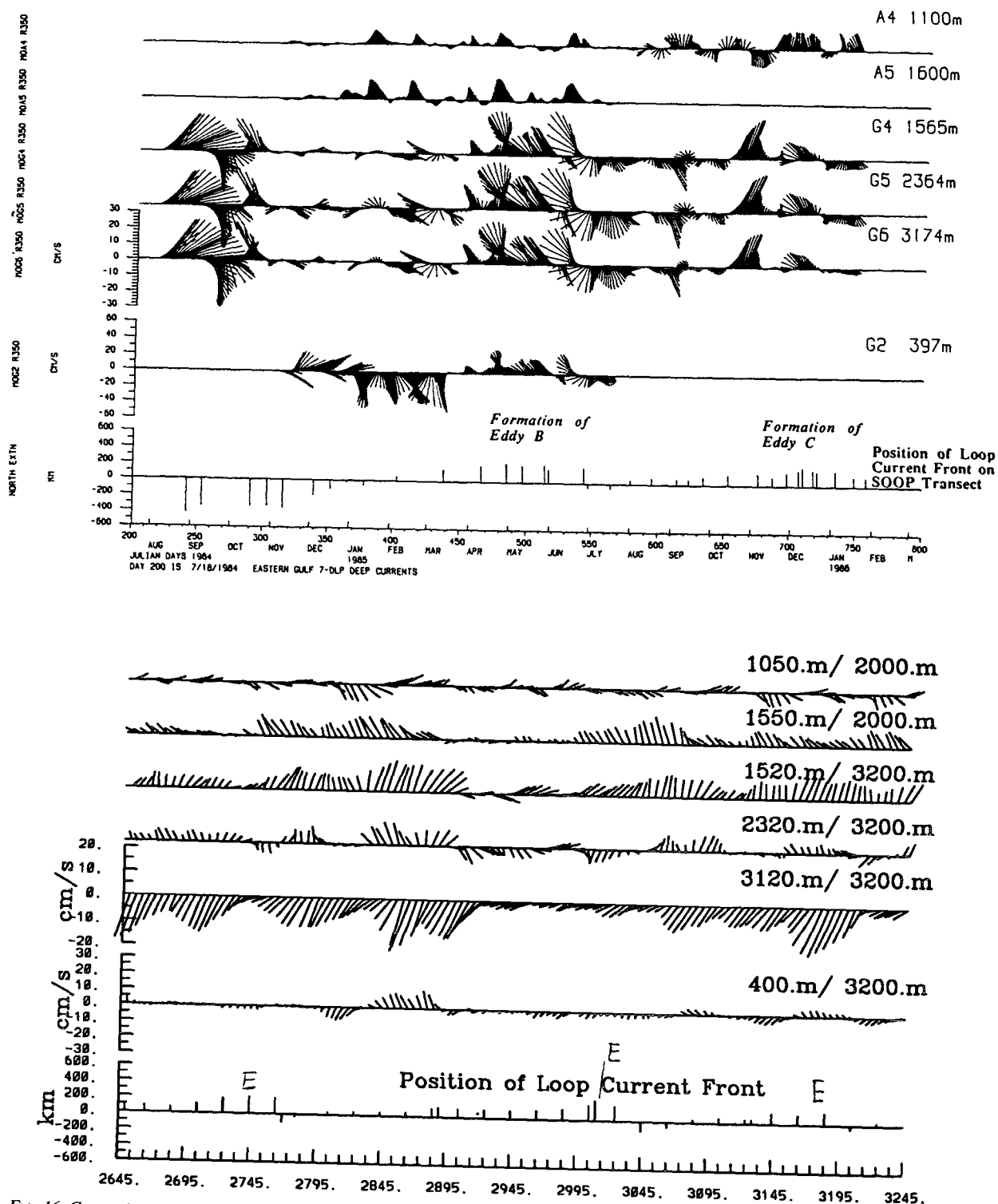


FIG. 16. Comparison of Hamilton's (1990; top panel) and model (lower panel; experiment C1) velocity stick plots at moorings A and G given in Table 2 (see also Fig. 1). Upward stick direction is  $10^\circ$  counterclockwise from true north. To indicate when eddies are formed, the position of the LC front along a transect from the Yucatan to the Mississippi Delta (Fig. 1) is also indicated. "E" indicates eddy formation in the model.

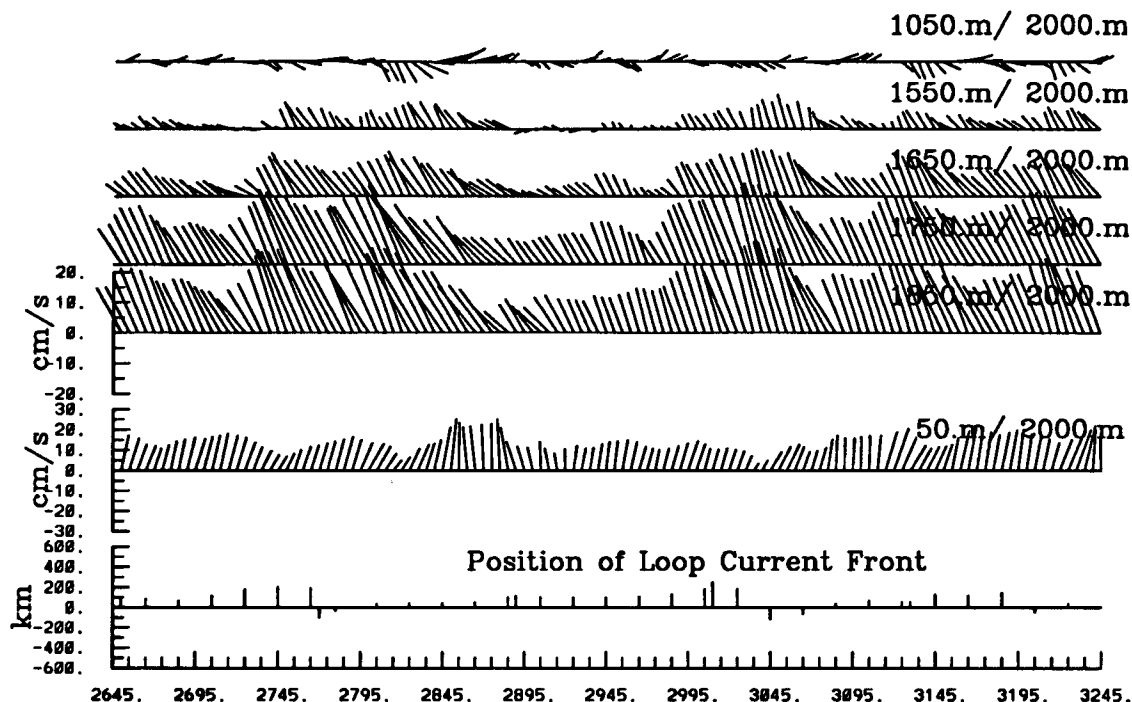


FIG. 17. Model (experiment C1) velocity stick plots at mooring Am (Fig. 1 and Table 2) showing the intensification of currents with depth.

(usually east–west) and minor (usually north–south) axes of the LCE, the maximum swirl transport of each eddy divided by 30 Sv—the specified steady inflow transport in the Caribbean, eddy westward propagation speeds, and initial and final longitudes and latitudes of eddy centers. These quantities are averaged over the total number of eddies for each experiment, and plotted in Fig. 11 (except experiment C5). In experiment C5 ( $C = 0.01$ ), no eddy sheddings occurred during the 3.3 years of integration, and results given below for experiments C3 ( $C = 0.05$ ) and C4 ( $C = 0.03$ ) suggest that the eddies would be rather small (diameter less than 200 km) and short lived (life span less than 100 days) if

they were shed after a longer integration. We will not consider experiment C5 further. To qualify as a LCE, the eddy must have a diameter of at least 100 km and a maximum swirl transport of at least 15 Sv (i.e., 50% of the total specified transport). The outer edge of an eddy (i.e., its size) is taken as where the near-surface velocity has decreased to a magnitude of 20% of its maximum, or about  $0.1 \text{ m s}^{-1}$ , and an eddy's life is considered terminated when its swirl transport has weakened to less than 6 Sv, or about 20% of its maximum immediately after shedding. These criteria are somewhat arbitrary but provide a basis for unbiased comparisons among the different experiments.

TABLE 2. Moorings for model and observed time series comparisons in Fig. 16.

Observation mooring	Latitude/longitude	Water depth (m)	Depth (m)	Model mooring	Latitude/longitude	Water depth (m)	Depth (m)
A	25°43'N 84°53'W	1700		Am	26°16'N 85°00'W	2000	
A4			1100	Am4			1050
A5			1600	Am5			1550
G	25°36'N 85°30'W	3200		Gm	26°16'N 85°11'W	3200	
G2			395	Gm2			400
G4			1565	Gm4			1520
G5			2365	Gm5			2320
G6			3174	Gm6			3120

For small  $C$  ( $=0.03$  and  $0.05$ ), the shedding period is long (about 400 days), primarily because many of the eddies are not qualified based on the above criteria. When they do qualify, they are of small sizes, with maximum major axes of about 200 km; weak, with maximum swirl transport of about 15–18 Sv; and tend to break up easily so that the life span is short, about 100 days. With increased  $C$ , the shedding periods decrease to about 220 to 280 days, in agreement with Sturges (1992), who found in the spectrum of LC variability a primary peak near 8.5 months (255 days). As  $C$  increases, the eddy life span, sizes, and % swirl transport increase to about 200 days, 300–400 km, and 80%–85%, respectively. These values are also in better agreement with those observed (Elliot 1982). Other eddy properties are fairly insensitive to “ $C$ .” The westward propagation speeds for all experiments fall within 3–4 km day<sup>-1</sup>, in good agreement with observations (Elliot 1982; Kirwan et al. 1984; Lewis and Kirwan 1987) and also with other model results (Hurlburt and Thompson 1980; Sturges et al. 1993). The modeled eddies are approximately circular, with ratios of the minor to major axes being in the range of 0.7–0.9. For all experiments, the LCEs traverse the Gulf in an almost straight westward path with small southward drift (about 20–60 km; Fig. 11f). In the case of experiment C4, the shedding latitude is some 60 km farther south, and there is a north-northwestward eddy excursion immediately after shedding, which results in a final latitude north of the initial latitude. Also, although we generally did not track eddies beyond 95°W, some wall and slope effects exist (Smith 1986; Oey 1995; see below). An example of the straight westward eddy drift is given in Fig. 12, which shows the tracks of some of the eddy centers for experiment C4. These are similar to the model results of Sturges et al. (1993; their Fig. 9). In the absence of appreciable ambient effects, including influences from other eddies, southward drift is induced by southward self-advection (i.e., nonlinearity) caused by the asymmetric pressure field around an eddy through Rossby wave dispersion (Smith and O’Brien 1983); the lack of such drift in the model may therefore be explained by weaker modeled currents.

In experiment C2A, all 30-Sv inflow is specified along the southwestern slope of the Caribbean Sea. The inflow is therefore more strongly controlled by topography. Hurlburt and Thompson’s (1980) results suggest that this inflow configuration will have the effect of suppressing eddy shedding, hence, increased shedding period and reduced swirl transport (the “X” in Figs. 11a,c), although the values are still within the observed range. In C2B in which all 30 Sv is specified through the eastern portion of the model boundary in the Caribbean, the reverse is true (not shown). All other eddy characteristics are not sensitive to these different inflow conditions, however. We conclude, therefore, given a value of  $C$  of about 0.075–0.1, the model results are fairly robust with respect to large changes

in the inflow conditions, and the resulting eddy characteristics are in fair agreement with those observed.

### c. Sensitivity of shelf circulation to Mississippi discharge location

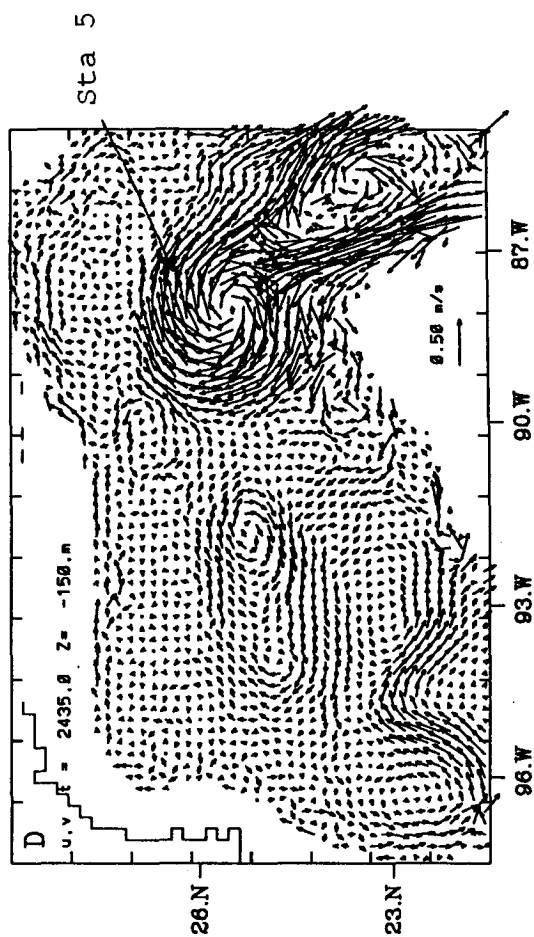
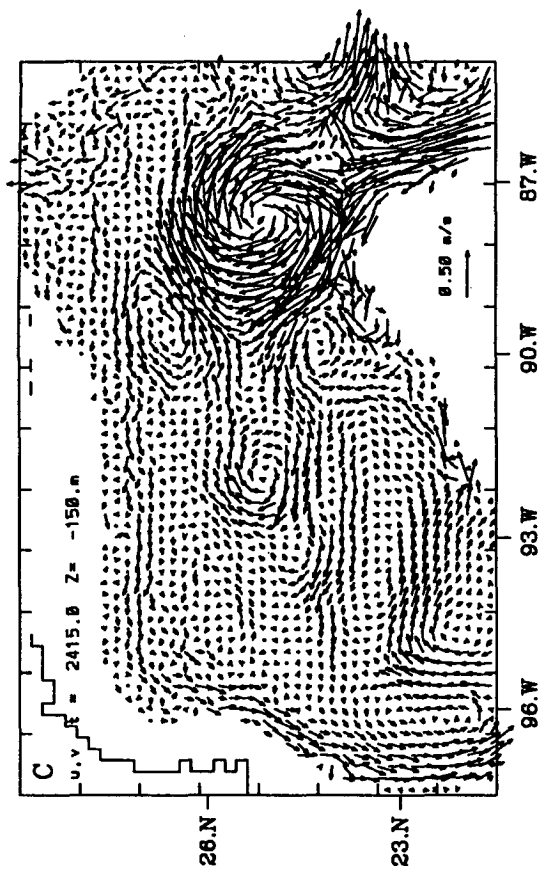
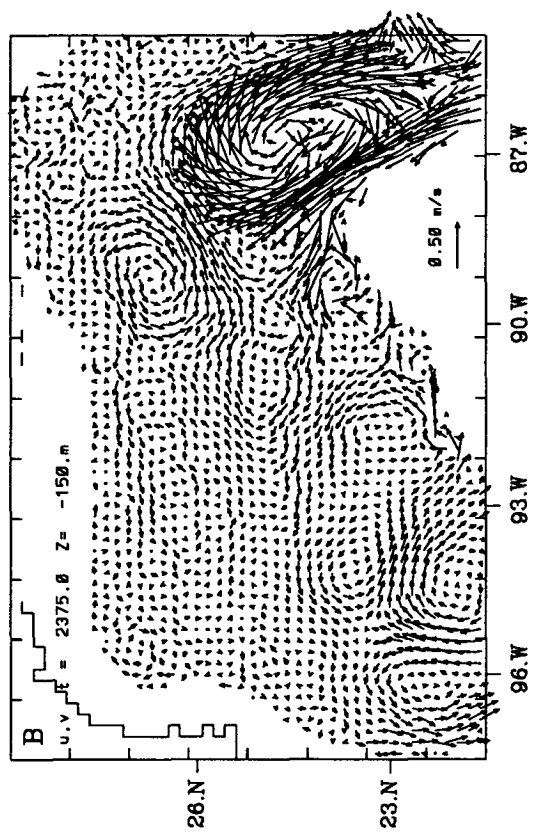
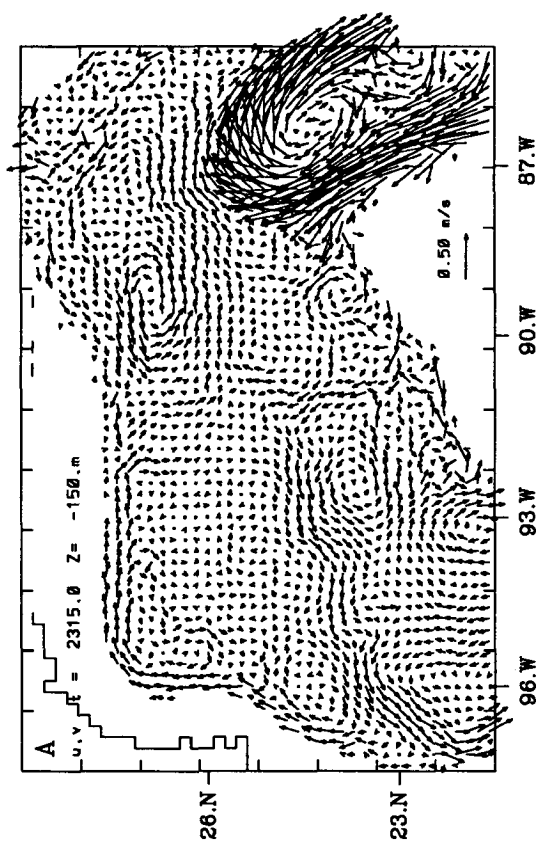
We examine results from experiment C2 prior to eddy shedding but after the LC is established. For discharge location east of the model delta (Fig. 13a), the plume veers eastward, contrary to what one might expect; that flow turns westward under the influence of the Coriolis force. Observations suggest that on the outer Alabama shelf and slope the flow is predominantly eastward driven by the LC (e.g., Schroeder et al. 1987). This eastward flow in the model (south of the delta; Fig. 5) was apparently sufficient to overcome the Coriolis effect. As a result, one only sees the effects of the Atchafalaya and Sabine Rivers over the LATEX shelf, and the nose of the buoyant coastal water reaches only to 27.5°N off the Texas coast, instead of to about 26°N as observed during winter (Cochrane and Kelly 1986). When the discharge location was shifted southward (beginning at  $t = 632$  days) by one grid point so that it now lies directly south of the model delta, the results (Fig. 13b–d) show a buoyancy-induced LATEX shelf salinity distribution more in accordance with observations. The response time (from Figs. 13b–d) is about 4 to 5 months, comparable to what one might infer from the salinity plots given in Cochrane and Kelly (1986); their plots show the beginning of a westward advection of less-saline water in October that continues through February in response to changing wind conditions. Clearly, the sensitivity of the modeled Mississippi outflow is due to the coarse grid used. However, it is also dynamically caused in that ambient flow in the region south of the delta is divergent. For all the experiments listed in Table 1, the “correct” discharge location of Fig. 13b was used.

## 4. Comparison with observations

The simplicity of the forcing in the calculation does not warrant an exhaustive comparison with observations. Nevertheless, some idea of how the modeled LCEs and related variability compare with data is of interest.

### a. Vertical section contours

Elliott’s (1982) section across a LCE shows a depression of the 20°C isotherm of about 140 m, while the modeled depression is about 120 m (Fig. 14). Observation shows the Caribbean subtropical underwater (SUW; salinity maximum: 36.6 ppt at 22.5°C) at about the 150–250-m depth, which is absent in the model. Modeled salinity in the Caribbean does indicate the existence of SUW (not shown), barely resolved by the near-surface sigma grid (usually the second grid) for regions where the water depths are greater than about



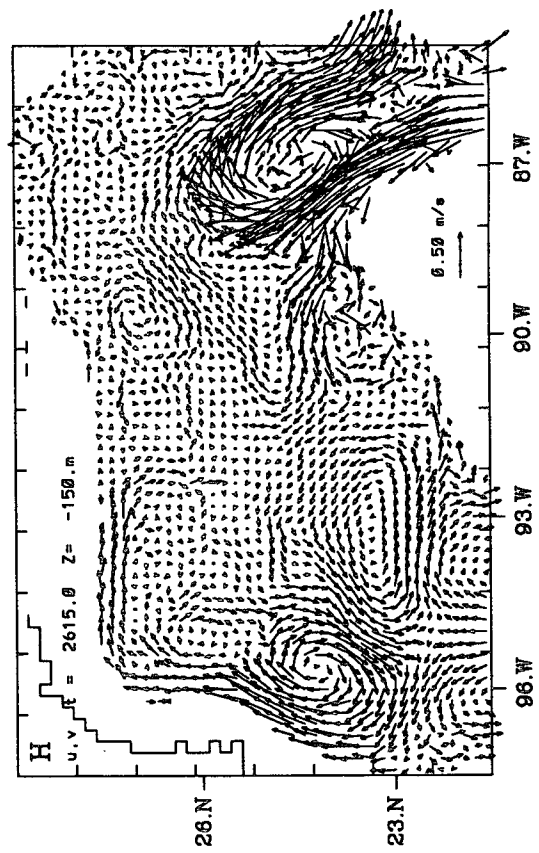
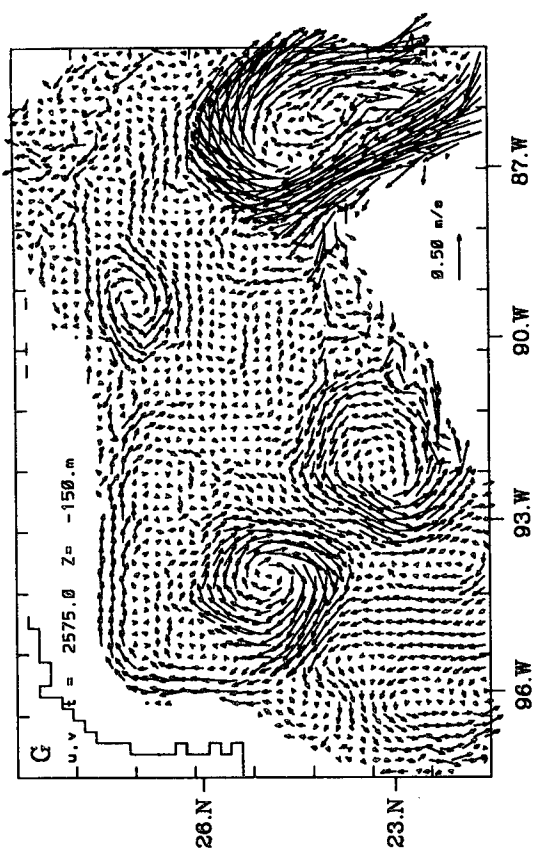
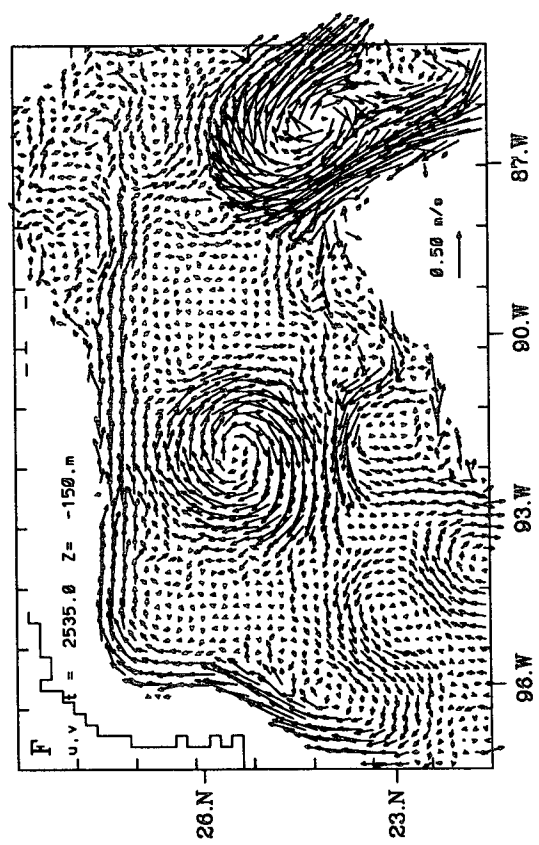
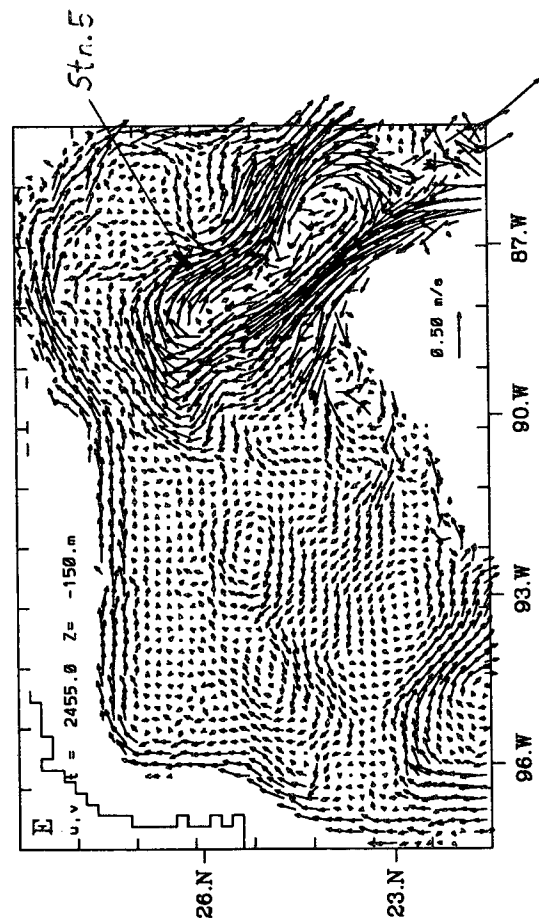
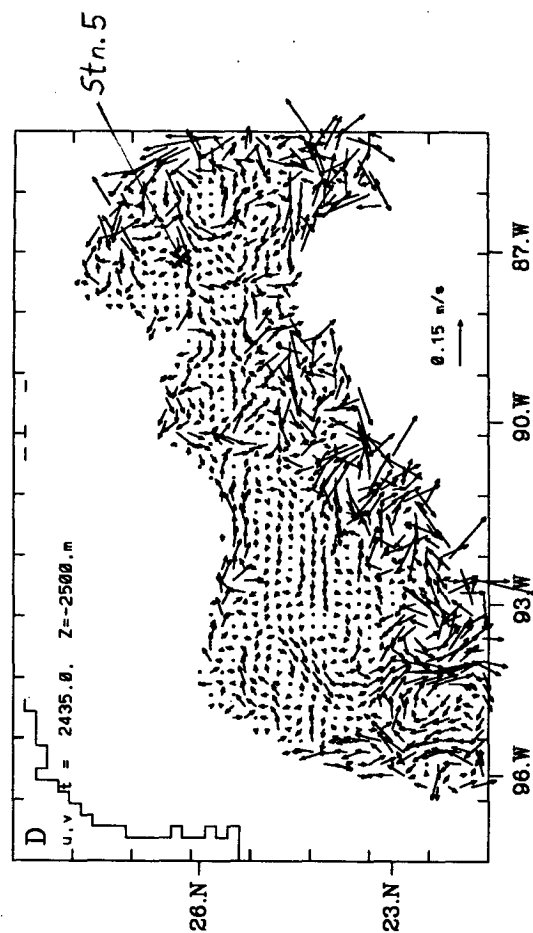
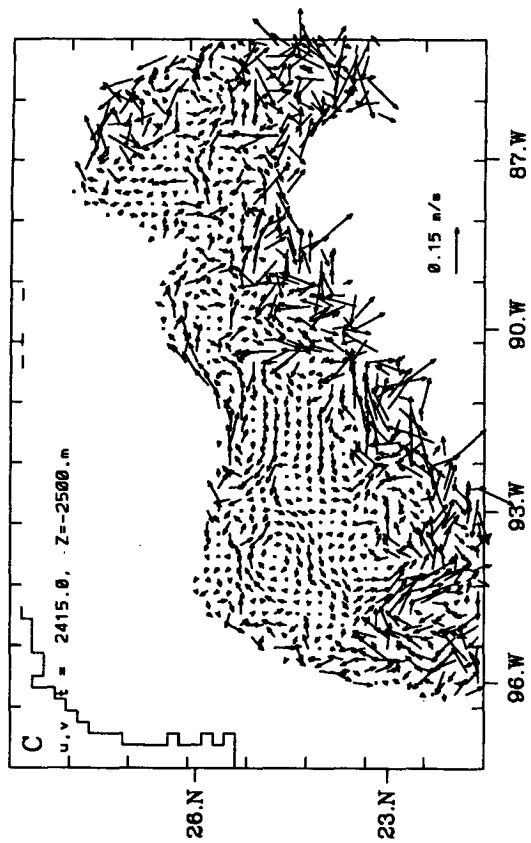
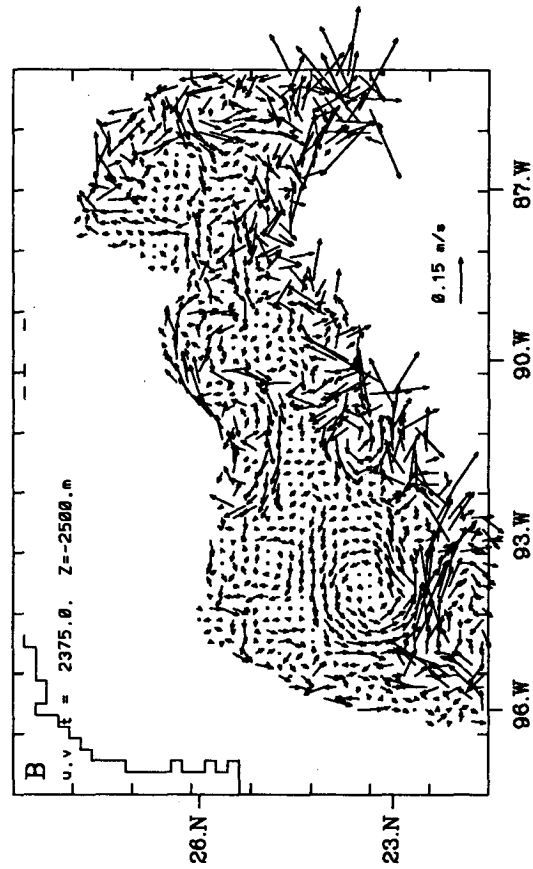
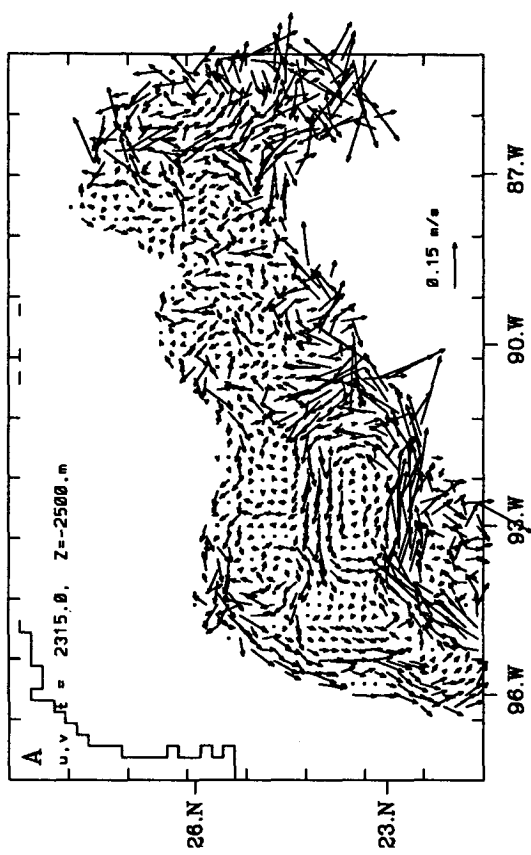


FIG. 18. Velocity vectors for model experiment C4 at  $z = -150$  m at various times of a LCE shedding and propagation for illustration of trapped wave propagation in the Gulf (see text).





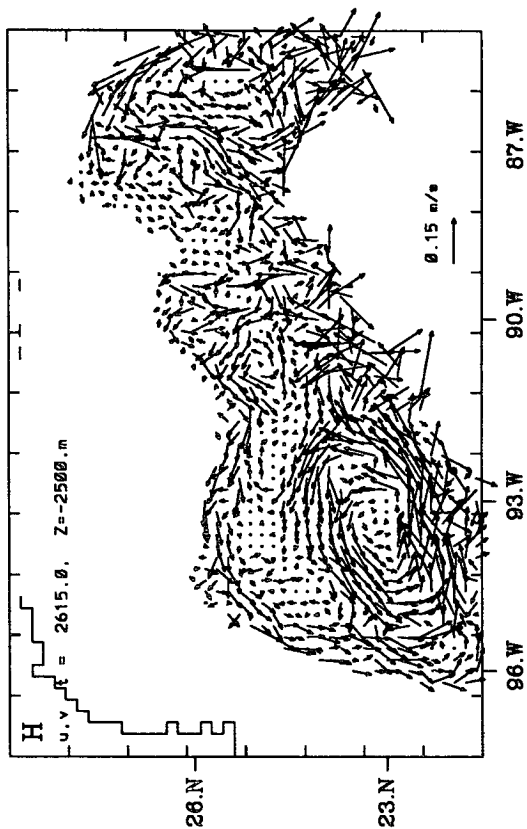
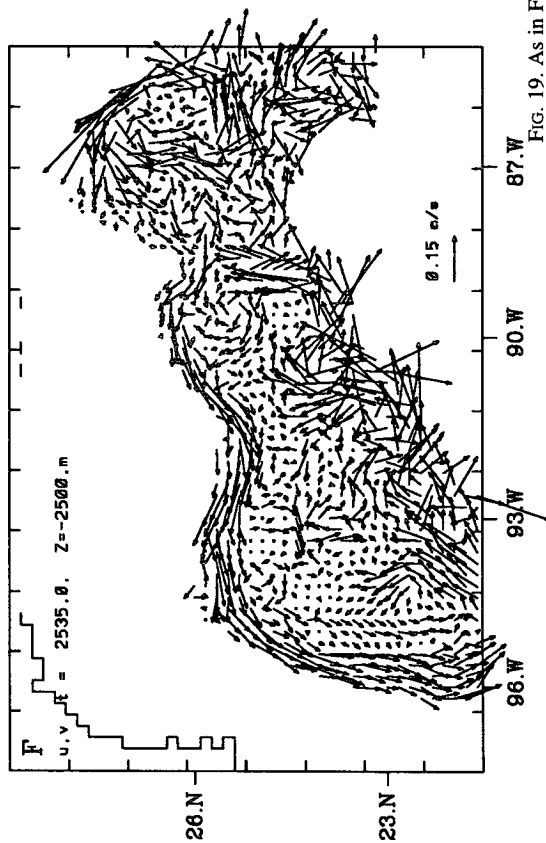
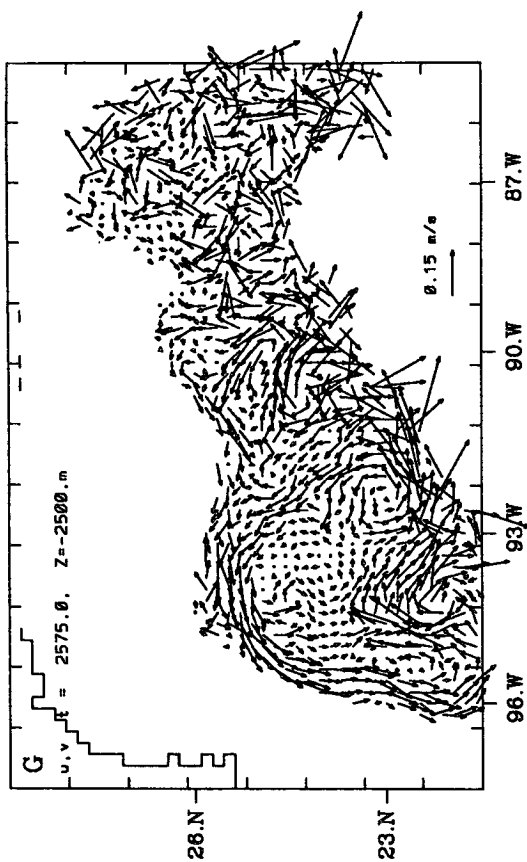
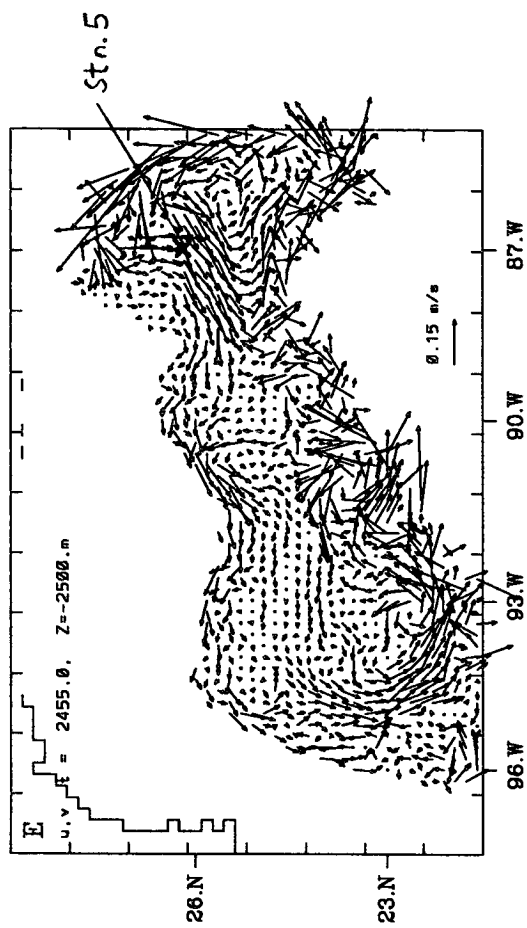


Fig. 19. As in Fig. 18 but for  $z = -2500$  m.

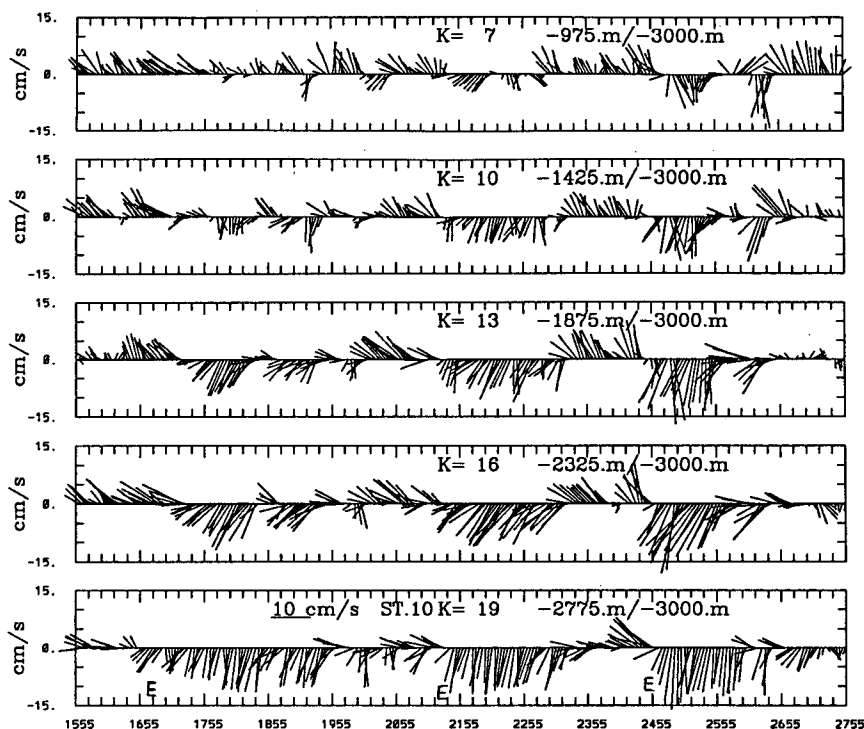


FIG. 20. Model (experiment C4) velocity stick plots at station 10 (Fig. 1) in the western Gulf showing the intensification of currents with depth. Upward stick direction is  $13^\circ$  clockwise from true north. Here, "E" in bottom panel indicates time of eddy shedding in the east.

2000 m. Upon entering the Gulf, the signal is almost entirely obliterated in the shed eddy.

The maximum simulated swirl (Fig. 14c) speed is about  $0.65 \text{ m s}^{-1}$  at the surface. This is weaker than the observed maxima of about  $0.88 \text{ m s}^{-1}$  (Elliott 1982) and  $1.7 \text{ m s}^{-1}$  (Forristal et al. 1992). The radial velocity indicates surface divergences at the outer edge of the eddy ( $x < 200 \text{ km}$  and  $x > 400 \text{ km}$ ) but both convergence and divergence near the center. Thus, there appears to be little frictional spindown for this low-viscosity experiment.

For experiment C1 (Fig. 15), the  $20^\circ\text{C}$  isotherm depression is about 80 m, some 30% less than for experiment C4 of Fig. 14. The maximum swirl speeds are also smaller, but the difference (about  $5 \text{ cm s}^{-1}$ ) is probably not significant. However, the radial velocity contours shows surface divergence at the eddy's center, suggestive of frictional spindown in this large viscosity case.

#### b. Time series

We compare (Figs. 16 and 17) the modeled currents with Hamilton's (1990) subsurface current time series at moorings A and G (Fig. 1) where variabilities were presumably dominated by dynamics driven by the LC and LCEs, and intercomparison is less ambiguous despite the fact that model simulations were not for any

specific dates. The model results are from experiment C1. Other experiments with smaller viscosities give similar results except the currents are 10% to 30% stronger. Also, model results were archived at only a limited number of stations in the Gulf and these in general differ from the observational mooring locations (Table 2 and Fig. 1). The nearest locations are used for comparison.

Hamilton (1990) noted a high degree of vertical coherence at both moorings A and G, and an increase in speed with depth. Currents (especially those at "G") tended to increase northward when eddies were formed (May 1985 and December 1986). Modeled currents show high vertical coherence at station Am (Fig. 17), but less at station Gm with current reversal at deeper levels (3120 m/3200 m in Fig. 16). Current speeds also increase with depth especially at Am, although the values (about 10 to  $20 \text{ cm s}^{-1}$ ) are less than those observed. The correlation between eddy formation and increased northward currents can be seen in the model time series, though the response is more gradual (i.e., not episodic as observed). The mean currents are northward about 3 to  $4 \text{ cm s}^{-1}$ , which can be compared with the observed means of about  $2 \text{ cm s}^{-1}$  at A4 and G4 (Hamilton's Fig. 15). These subsurface northward currents correspond to the eastern side of the quasi-permanent cyclonic recirculation off the West Florida Shelf (cf.

the streamfunction plots in Fig. 5). Thus, the cyclone strengthens when eddies are shed.

Sturges et al. (1993) found vertically coherent modeled currents (mooring G) for levels deeper than about 1000 m. However, the direction was southward at all levels except during one instant of eddy shedding, when deep-level currents reversed (northward) with magnitudes of about  $1\text{--}2\text{ cm s}^{-1}$ .

### c. Topographic Rossby wave

Hamilton (1990) suggested that the observed increase with depth of the current intensity is indicative of TRW. He also suggested that these waves are generated in the eastern Gulf as a result of LC expansion and contraction, and that they subsequently propagate westward at a speed of about  $9\text{ km day}^{-1}$ . Deep currents in the western Gulf typically intensify southward as a result of TRW (see Hamilton's Fig. 11 at mooring Q4). However, arrivals of eddies in the western Gulf also often produce deep southward current events (Hamilton 1990; Sturges et al. 1993, their Fig. 11), and it can be difficult to differentiate between the two phenomena. By way of velocity vector plots (snapshots) and time series analyses (spectra and coherency), I show below nonlocal responses indicative of TRW generation and propagation in the model deep levels.

#### 1) VELOCITY VECTOR PLOTS

Figures 18 and 19 show plots from experiment C4 at  $z = -150\text{ m}$  (Fig. 18) and  $-2500\text{ m}$  (Fig. 19), starting from  $t = 2315$  days when the remnant of a previously shed (already decayed) eddy in the western Gulf can be seen. The current over the western slope is northward north of  $23^\circ\text{N}$  near the surface and southward near the bottom (Figs. 18a and 19a)—a locally forced response expected from the results of Hamilton and Sturges et al. Figure 18a also shows a near-surface, north–south splitting of the current (at  $23^\circ\text{N}$ ) as a result of eddy collision on the western slope [a feature observed by Vidal et al. (1992)]. There was little activity in the western slope after the locally forced response subsided (Figs. 18b, 19b).

An LCE-shedding event begins at  $t = 2375$  days, preceded by a cyclone northwest of the LC. The cyclone generates surface-intensified, slope-bound (isobath  $< 1000\text{ m}$ ) currents that extend to the bottom (not shown; no signature of the current at  $z = -2500\text{ m}$ , Figs. 19b,c) and propagate around the basin (Fig. 18c) with speeds of about  $0.5$  to  $1\text{ m s}^{-1}$ , the characteristic of a coastally trapped wave (CTW) solution (Gill and Clarke 1974) taking the shelfbreak as the “coast.”

Figures 19d through 19f illustrate the clearest evidence to date of TRW generation and propagation simulated from a Gulf of Mexico model with realistic topography. Figures 18d and 18e show the LC in the process of being “pinched off” in the vicinity of sta-

tion 5 at  $26^\circ\text{N}$ ,  $87^\circ\text{W}$  (see Fig. 1), where at  $-2500\text{ m}$  the currents intensify west-southwestward (approximately along local isobaths; Figs. 19d and 19e). The intensification occurred prior to LCE shedding (Figs. 18e and 19e), and is therefore produced by a LC northward expansion as well as by shedding. Figures 19d and 19e also show intensifications of north-northwestward deep currents along the Florida slope, and these precede the westward currents at station 5 (cf. Fig. 19c with 19d and 19e). Slope-bound currents are again generated through CTW propagation, reversed in direction from that previously generated by the cyclone (Figs. 18d,e; speeds about  $0.5$  to  $1\text{ m s}^{-1}$ ). Although near-bottom slope currents are evident in Fig. 19e, their dominance off the LATEX shelf and in the western Gulf is seen only some 40 to 100 days later (Fig. 19f), which gives a westward propagation speed of about  $0.1$  to  $0.2\text{ m s}^{-1}$  ( $8$  to  $20\text{ km day}^{-1}$ ). The apparent propagation speeds are larger than what might be induced by a pure TRW propagation [about  $9\text{ km day}^{-1}$ , Hamilton (1990)], due perhaps to both free and forced solutions. Figure 19f illustrates the “trapped” nature of the current: intense close to the slope and rapid decay offshore over distances of about 100 to 150 km. At this time, the LCE is located in the mid-gulf (Fig. 18f), and the western gulf current response is clearly nonlocal. As the LCE collides with the western slope (Figs. 18g,h and 19g,h), the locally generated slope currents are northward near the surface and southward at  $z = -2500\text{ m}$  (cf. Figs. 18a and 19a).

#### 2) TIME SERIES AND SPECTRA

Stick plots at station 10 (Fig. 1) in the western gulf show intensification of currents with depth (Fig. 20; other stations are similar) and also the effects of three LCE shedding events, the last of which corresponds to plots shown in Figs. 18 and 19. The first two eddies actually disintegrated and dissipated before reaching the western Gulf, so that the perturbations in Fig. 20 are nonlocally forced by sheddings in the east. These bottom intensification events are similar to those found in the stick plot shown in Hamilton [(1990) his Fig. 5, stations Q3 and Q4 over the 3000-m isobath in the western Gulf, in particular]. Thus, in addition to being trapped against the slope, the currents are also bottom trapped, strongly suggestive of a TRW response.

The kinetic energy (KE) spectra (Fig. 21) in the eastern gulf sta 3 (near Hamilton's mooring G) and sta 5 (where modeled eddies are shed; Fig. 18) show intensification with depth at frequencies 0.01, 0.02, and 0.03 cpd (sta 3), and 0.02–0.03 cpd (sta 5). At station 5, peaks also occur at frequencies 0.013 and 0.04–0.05 cpd for  $z < -1275\text{ m}$ , and over a fairly broad frequency band from 0.003 to 0.006 cycles per day (cpd) near the surface. The latter is caused by LC variabilities and LCE sheddings at periods of 170–330 days. Not all of LC expansion and contraction events

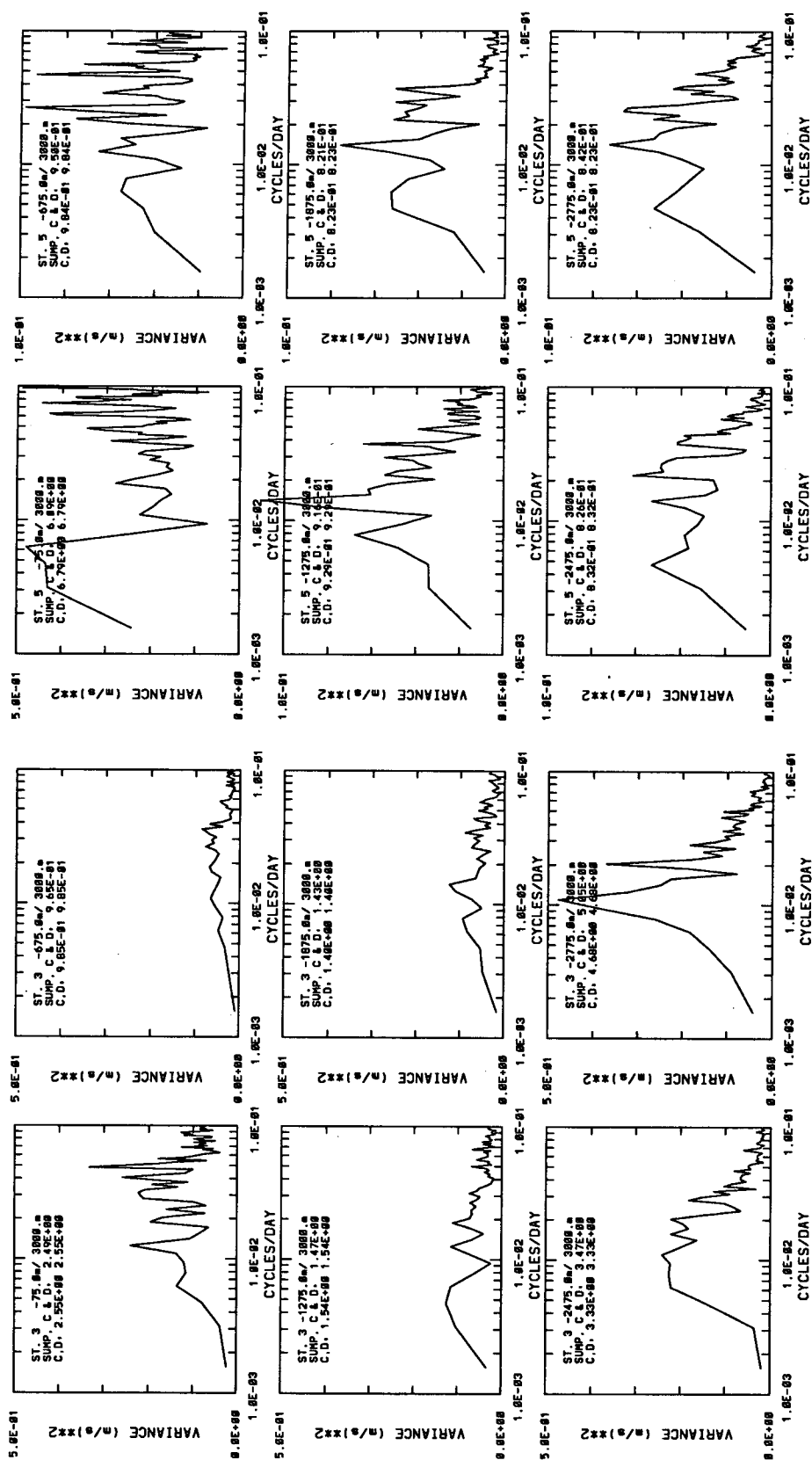


FIG. 21. Kinetic energy spectra in variance-preserving form at various depths at stations (a) 3, (b) 5, (c) 8, and (d) 10 on the 3000-m isobath (see Fig. 1 for station locations). The time series is year 4.3 through 8.6 (320 data points, 5 days per point, segmented into five 64 points) of experiment C4. The KE spectrum is defined as half the sum of the spectra for the along- and across-isobath components.

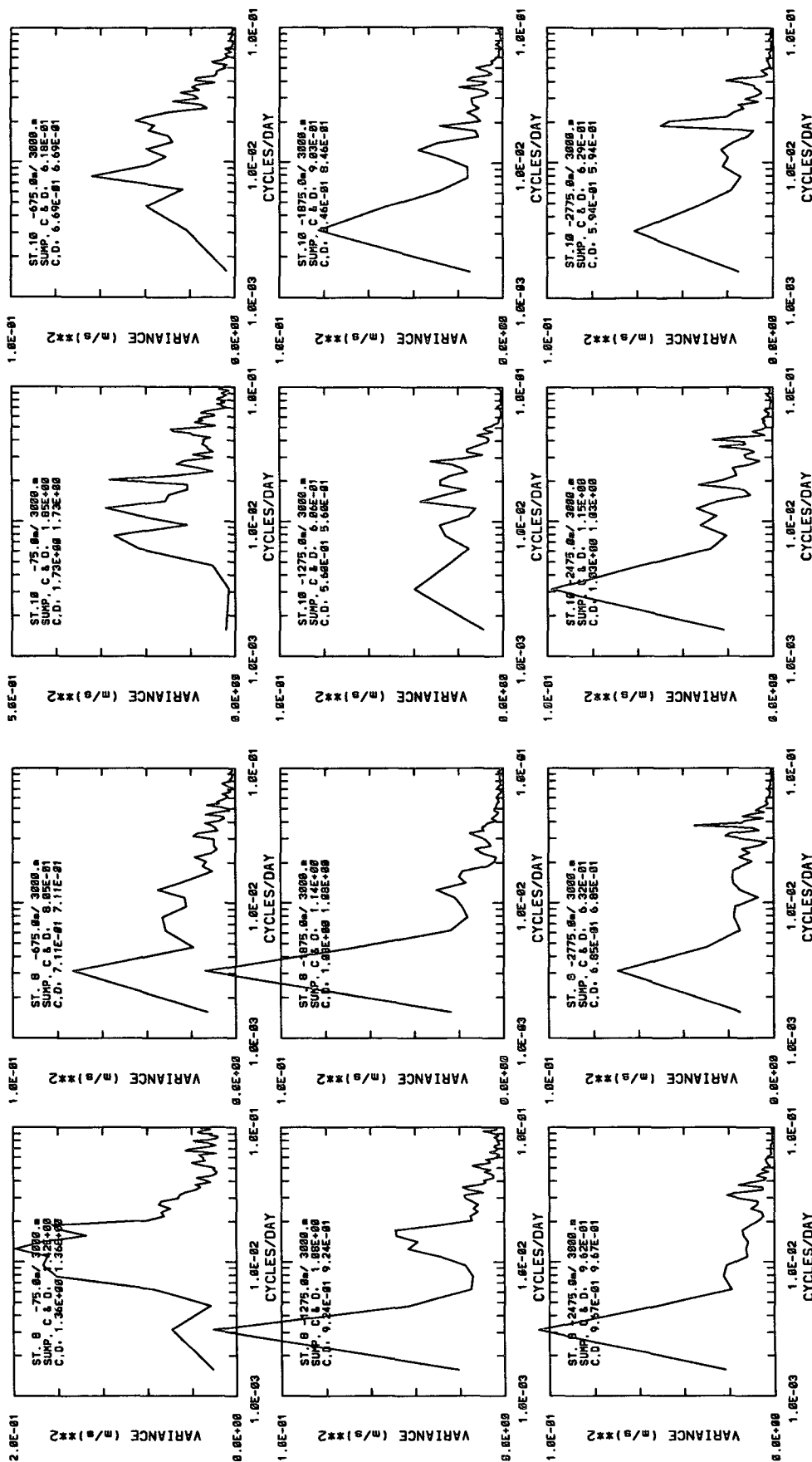


FIG. 21. (Continued)

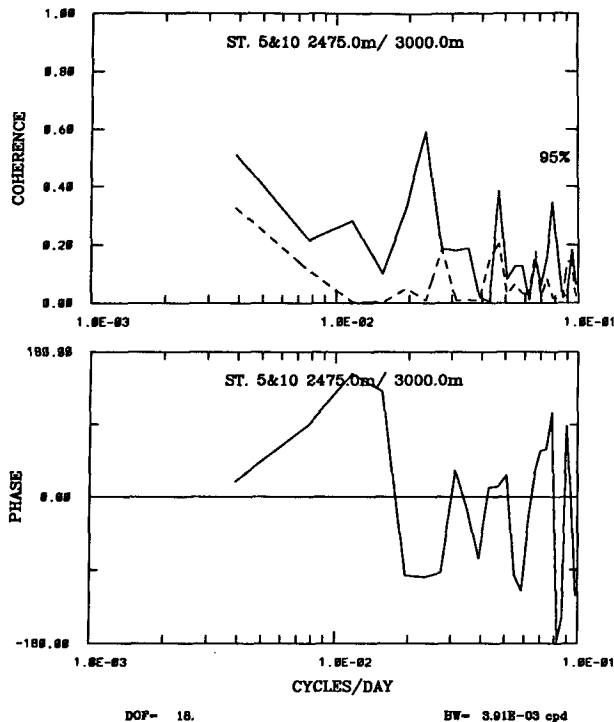


FIG. 22. Coherence squared (95% significance curve is shown in dashed) and phase between stations 5 and 10 for experiment C4. A lag of 60 days had been applied to station 10 in anticipation of the 10 km day<sup>-1</sup> TRW propagation speed.

led to eddy shedding, which gives rise to peaks at higher frequencies than the LCE shedding frequency of about 0.0025 cpd for experiment C4 (Fig. 11). There is also a peak at 0.008 cpd at station 5 from near surface to about mid-depth; this corresponds to the CTW mode, but its signature at the surface may be masked by the more intense LC variabilities and LCE sheddings (see below for sta 8 and 10). The frequencies of deeper-level KE peaks are in good agreement with those observed by Hamilton (1990), who found spectral peaks at 0.04, 0.02–0.03, and 0.01 cpd in the eastern gulf. While the near-surface spectra at station 5 show a number of peaks for frequencies greater than about 0.05 cpd, the shape is quite different from the corresponding spectra at deeper levels; the latter show quite abrupt KE drops for frequencies greater than 0.05 cpd, despite the possible aliasing errors near the Nyquist frequency of 0.1 cpd. These results suggest a TRW behavior for which a cutoff frequency of about 0.06 cpd is estimated from the model topography and density field (cf. Hamilton 1990).

Farther west at stations 8 and 10, KE peaks occur near 0.003, 0.012 (sta 10 only), 0.02 (sta 10 only), and 0.04 cpd. The last three of these intensify with depth and are within the frequency range characteristic of TRWs observed by Hamilton (1990). The CTW mode of 0.008 cpd now appears from the surface to

mid-depth, especially at station 10 (this mode extends to the bottom for stations at 2000-m isobath—not shown). The lowest mode at 0.003 cpd intensifies near mid-depth and is absent for the two near-surface grids at station 10. This mode corresponds to the first baroclinic Rossby wave basin mode, with period  $T_R \approx L_G / C_{Ri}$ , where  $L_G \approx 1500$  km, the basin's width, and  $C_{Ri} \approx 0.04$  m s<sup>-1</sup>, the internal Rossby wave phase speed; thus  $T_R \approx 350$ –400 days. Near the surface, the peak is caused by LCE passages, with a period of about 400 days. However, for experiment C4, not all of the LCEs reach the western Gulf, hence no near-surface peak at this lowest-frequency mode at station 10 (nor at sta 9; not shown).

The lack of direct eddy influence in the west (sta 9 and 10) makes the interpretation of higher-frequency responses there unambiguous in terms of TRW propagation from the east. The coherence squared between stations 5 and 10 at  $z = -2475$  m (Fig. 22; other near-bottom levels are similar) shows a significant peak at 0.022 cpd, as well as other lesser peaks at 0.04 to 0.05 cpd. At 0.022 cpd, station 10 lags station 5 by about 70 days. This gives a phase speed of about 12 to 13 km day<sup>-1</sup> (cf. estimates from Fig. 19) in fair agreement with Hamilton's (1990) estimate of 9 to 10 km day<sup>-1</sup>.

The above inferences about the existence of TRWs in the model (KE intensification with depth for frequencies 0.01 cpd and higher, and phase speed) hold true also for other experiments. Moreover, with a longer time series for experiment C2 and a shorter shedding period (about 220 days) distinct from that of the first baroclinic Rossby basin mode (about 400 days), a spectral peak that maximizes just below the main thermocline ( $z \approx -1000$  m; see Figs. 21c,d at 0.003 cpd) was confirmed, hence the baroclinic nature of the mode.

## 5. Summary

To the best of my knowledge, this is the first time the solution obtained from the Blumberg–Mellor model has been thoroughly documented for its dependency on the Smagorinsky constant and for the resulting effects on large-scale current and eddy fields. For too small lateral viscosity, the current and eddies tend to break up rapidly (in a matter of weeks) into small-scale, apparently incoherent features. For large viscosity, the current field is smooth with little eddy activity. For some intermediate viscosity, which for the present 20 km × 20 km horizontal grid size is about 200–400 m<sup>2</sup> s<sup>-1</sup> (Smagorinsky's constant  $\approx 0.1$ ), LCEs are produced with reasonable characteristics—average shedding period of about 250 days and eddy diameters of about 300 to 400 km. The dependence of the modeled LC and LCE on horizontal viscosity and diffusivity is a function of model grid sizes. In estuaries with high resolution [0.5 km × 0.5 km grid sizes; Oey et al. (1985)], we have used zero horizontal viscosity and

diffusivity. In the present Gulf of Mexico model, we also expect less sensitivity as horizontal resolution increases.

For a given Smagorinsky constant, the LCE shedding periods are not constant, despite the fact that other forcing like inflows, winds, and surface fluxes are held constant. It may be that a ten-year integration is still not sufficient for the system to settle into a quasi-equilibrium state. On the other hand, given the relatively rapid baroclinic adjustment time of  $O(3)$  years, the variable eddy shedding period (also observed) is more likely due to the variable Smagorinsky mixing, which on average yields a small lateral viscosity in the model Gulf.

Model results also suggest that inclusion of at least part of the Caribbean Sea may be necessary in modeling the LC dynamics. Transport variabilities through the Yucatan Channel are linked to LCE sheddings, which suggests that model boundary specifications at the Yucatan Channel may lead to spurious dynamics.

The LC variabilities, plus LCE sheddings, produce a number of important responses in the western Gulf. At the period of about 400 days, a baroclinic Rossby basin mode was found. This appeared at the surface but was most clearly seen just below the main thermocline at  $z \approx -1000$  m. There also exist near-surface responses at the LCE arrival period of about 250 days, as well as at the slope-bound CTW period of about 125 days caused by LC expansions and contractions. At shorter periods of between 30 and 100 days, bottom-intensified currents characteristic of TRWs occurred.

The present study is modest in scope because of the somewhat idealized forcings used. Future studies should employ more realistic forcings and, in conjunction with the LATEX study, direct comparison with in situ observations. In general, the model results underpredict the currents, both in the means and variances. The discrepancies may be because of coarse resolution, but they may also be due to the idealized forcings used.

**Acknowledgments.** I am indebted to Chris Mooers for his encouragements and constructive comments. Peter Niller suggested the sensitivity study on horizontal mixing. Y. Zhang did the graphics. This work was funded by the Mineral Management Service (COTR: Bob Labelle) via Dynalysis of Princeton, Inc. Supercomputer time was provided by the Pittsburgh Supercomputing Center and the National Center for Supercomputing Applications, Illinois.

#### REFERENCES

- Blumberg, A. F., and G. L. Mellor, 1983: Diagnostic and prognostic numerical circulation studies of the South Atlantic Bight. *J. Geophys. Res.*, **88**, 4579–4592.
- Burkov, V. A., L. I. Galerkin, and A. B. Zubin, 1982: New data on water exchange through the Yucatan Strait (in Russian). *Dokl. Akade. Nauk SSSR*, **265**(1), 190–195. [Available as a translation from *Oceanology*, 1984, 198–200.]
- Cochrane, J. D., and F. J. Kelly, 1986: Low frequency circulation on the Texas–Louisiana continental shelf. *J. Geophys. Res.*, **91**, 10 645–10 659.
- Elliott, B. A., 1982: Anticyclonic rings in the Gulf of Mexico. *J. Phys. Oceanogr.*, **12**, 1292–1309.
- Forristall, G. Z., K. J. Schaudt, and C. K. Cooper, 1992: Evolution and kinematics of a Loop Current eddy in the Gulf of Mexico during 1985. *J. Geophys. Res.*, **97**, 2173–2184.
- Gill, A. E., 1982: *Atmosphere–Ocean Dynamics*. Academic Press, 662 pp.
- , and A. J. Clarke, 1974: Wind-induced upwelling, coastal currents and sea-level changes. *Deep-Sea Res.*, **21**, 325–345.
- Hamilton, P., 1990: Deep currents in the Gulf of Mexico. *J. Phys. Oceanogr.*, **20**, 1087–1104.
- Hellerman, S., and M. Rosenstein, 1983: Normal monthly windstress over the world ocean with error estimates. *J. Phys. Oceanogr.*, **13**, 1093–1104.
- Hurlburt, H. E., and J. D. Thompson, 1980: A numerical study of Loop Current intrusions and eddy shedding. *J. Phys. Oceanogr.*, **10**, 1611–1651.
- Kirwan, A. D., W. J. Merrell, J. K. Lewis, R. E. Whitaker, and R. Legeckis, 1984: A model for the analysis of the drifter data with an application to a warm core ring in the Gulf of Mexico. *J. Geophys. Res.*, **89**, 3425–3438.
- Levitus, S., 1982: *Climatological Atlas of the World Ocean*. NOAA Prof. Paper 13, U.S. Dept. of Commerce, NOAA, Rockville, MD, 173 pp.
- Lewis, J. K., and A. D. Kirwan, 1987: Genesis of a Gulf of Mexico ring as determined from kinematic analyses. *J. Geophys. Res.*, **92**, 11 727–11 740.
- Maul, G. A., D. A. Mayer, and S. R. Baig, 1985: Comparison between a continuous three-year current meter observation at the sill of the Yucatan Strait, satellite measurements of Gulf Loop Current area, and regional sea level. *J. Geophys. Res.*, **90**, 9089–9096.
- Mellor, G. L., 1991: An equation of state for numerical models of oceans and estuaries. *J. Atmos. Oceanic Technol.*, **8**, 609–611.
- , and T. Yamada, 1982: Development of a turbulence closure model for geophysical fluid problems. *Rev. Geophys. Space Phys.*, **20**, 851–875.
- Oey, L.-Y., 1995: Eddy and wind-forced shelf circulation. *J. Geophys. Res.*, **100**, 8621–8637.
- , and P. Chen, 1992: A model simulation of circulation in the north-east Atlantic shelves and seas. *J. Geophys. Res.*, **97**, 20 087–20 115.
- , G. L. Mellor, and R. I. Hires, 1985: A three-dimensional simulation of the Hudson–Raritan estuary. Part I: Description of the model and model simulations. *J. Phys. Oceanogr.*, **15**, 1676–1692.
- Schroeder, W. W., S. P. Dinnel, W. J. Wiseman Jr., and W. J. Merrell Jr., 1987: Circulation patterns inferred from the movement of detached buoys in the eastern Gulf of Mexico. *Contin. Shelf Res.*, **7**, 883–894.
- Smagorinsky, J., 1963: General circulation experiments with the primitive equations. Part I: The basic experiment. *Mon. Wea. Rev.*, **91**, 99–164.
- Smith, D. C., IV, 1986: A numerical study of Loop Current eddy interaction with topography in the western Gulf of Mexico. *J. Phys. Oceanogr.*, **16**, 1260–1272.
- , and J. J. O'Brien, 1983: The interaction of a two-layer isolated mesoscale eddy with topography. *J. Phys. Oceanogr.*, **13**, 1681–1697.
- Sturges, W., 1992: The spectrum of Loop Current variability from gappy data. *J. Phys. Oceanogr.*, **22**, 1245–1256.
- , J. C. Evans, S. Welsh, and W. Holland, 1993: Separation of warm core rings in the Gulf of Mexico. *J. Phys. Oceanogr.*, **23**, 250–268.
- Vidal, V. M., F. V. Vidal, and J. M. Perez-Molero, 1992: Collision of a Loop Current anticyclonic ring against the continental shelf slope of the western Gulf of Mexico. *J. Geophys. Res.*, **97**, 2155–2172.
- Vukovich, F. M., B. Crissman, M. Bushnell, and W. King, 1979: Some aspects of the oceanography of the Gulf of Mexico using satellite and in situ data. *J. Geophys. Res.*, **84**, 7749–7760.